Chemical Engineering Science 305 (2025) 121133

Contents lists available at ScienceDirect

Chemical Engineering Science

journal homepage: www.elsevier.com/locate/ces

Experimental study and modeling of a droplet CO_2 absorber for the carbon-negative soda ash production

Maria F. Gutierrez [a,*], Kasimhussen Vhora [a,b], Somayyeh Ghaffari [a], Gábor Janiga [b], Andreas Seidel-Morgenstern [a], Heike Lorenz [a], Peter Schulze [a]

[a] Max Planck Institute for Dynamics of Complex Technical Systems, Sandtorstr. 1, 39106 Magdeburg, Germany
[b] Otto von Guericke University, Universitätsplatz 2, 39106 Magdeburg, Germany

ARTICLE INFO

Keywords:
Carbon dioxide
Absorption
Capture rate
Energy consumption

ABSTRACT

As part of a new environmental-friendly and carbon-negative process for soda ash production, the use of a novel droplet absorber for the Direct Air Capture (DAC) of CO_2 with NaOH solutions is studied experimentally and by concomitant process modeling. Two different nozzle plates with different number of holes are tested, and the counter-current and co-current arrangements are evaluated in terms of change of CO_2 concentration, capture rate and energy consumption. In the co-current operation, the fall of small droplets drives the flow of air inside the absorber and no fan is required. The effect of the liquid flow rate, the CO_2 inlet concentration, the gas velocity, the temperature and the liquid concentration is quantified. Two models are compared: one neglecting and the other considering droplet coalescence using CFD simulations. The inclusion of the force balances in the model allowed proper description of the fluid velocities and specific surface area inside the droplet absorber. Due to the high specific surface areas obtained (100–400 m^2/m^3), the studied droplet absorber outperforms reported spray absorbers for CO_2 capture. The capture rate is in the range between 0.7 and 2.4 kg CO_2/(h-m^3 absorber) and the energy consumption between 248 and 1008 kWh/(t CO_2), depending on the operational conditions. The performance and practical implementation of the droplet absorber in comparison with standard absorbers for DAC applications are discussed.

1. Introduction

Among the mitigation pathways with potential to limit global warming is the development of near zero CO_2 emission industries. Moreover, Carbon Dioxide Removal (CDR) technologies, which remove CO_2 directly from the atmosphere (Direct Air Capture, DAC), play a major role in many mitigation scenarios. However, some technical limitations should be overcome before CDR techniques can be applied to reduce atmospheric greenhouse gas levels (IPCC, 2023). As a response, the CODA project aims to develop a new sustainable and carbon-negative process to produce calcined soda ash (sodium carbonate) from rock salt brine and atmospheric CO_2 (BMBF (Bundesministerium für Bildung und Forschung) and FONA (Forschung für Nachhaltigkeit) (2023)). For this, a sodium hydroxide solution is produced by electrolysis of a salt brine solution using renewable energy. Then, the alkaline solution is used to capture CO_2 directly from air in an absorber, where the reaction shown in Equation (1) is taking place in the liquid phase. The carbonated solution out of the absorber is fed to a crystallization downstream processing train to obtain anhydrous soda ash. Unlike the traditional process (Solvay process), the CODA process is carbon-negative because the captured CO_2 is used as source of carbonate ion in the product and it uses renewable energies.

$$CO_{2(aq)} + 2NaOH_{(aq)} \leftrightarrow Na_2CO_{3(aq)} + H_2O \quad (1)$$

For the feasibility of the described process, specific studies on the optimal design of the CO_2 absorption unit should be done to ensure its minimal energy consumption. In literature, the main studied reactor technologies using a NaOH solution as sorbent are packed columns (Baciocchi et al., 2006; Holmes and Keith, 2012; Mahmoudkhani and Keith, 2009; Mazzotti et al., 2013; Zeman, 2008), spray columns (Bandyopadhyay and Biswas, 2012; Dimiccoli et al., 2000; Stolaroff et al., 2008; Tamhankar et al., 2015) and bubble columns (Azizi et al., 2022; Gaur et al., 2009; Pichler et al., 2021; Shim et al., 2016; Tavan and Hosseini, 2017; Yoo et al., 2013). Since the CO_2 concentration in air is very small (~ 400 ppm), the absorption of CO_2 directly from air would require to process very large volumes of air. Therefore, capture

* Corresponding author.
E-mail address: gutirrezsnchez@mpi-magdeburg.mpg.de (M.F. Gutierrez).

https://doi.org/10.1016/j.ces.2024.121133
Received 4 April 2024; Received in revised form 1 November 2024; Accepted 20 December 2024
Available online 25 December 2024

Nomenclature

a	Specific mass transfer area per volume of absorber (m^2/m^3)
a_e	Effective specific mass transfer area per volume of absorber (m^2/m^3)
A	Cross sectional area of the absorber (m^2)
A^{top}	Cross sectional area at the top of the set-up where the velocity was measured (m^2)
$c^*_{CO_2}$	Concentration of CO_2 in the liquid phase in equilibrium with the bulk gas phase concentration of CO_2 ($kmol/m^3$)
c_{CO_2}	Molar concentration of CO_2 in the bulk liquid phase ($kmol/m^3$)
$c^i_{CO_2}$	Molar concentration of CO_2 in the interface liquid phase ($kmol/m^3$)
c_i	Concentration of the component i ($kmol/m^3$)
c_w	Molar concentration of water in the liquid phase ($kmol/m^3$)
c_L	Molar concentration of the liquid phase ($kmol/m^3$)
c_{Na^+}	Molar concentration of sodium ion in the liquid phase ($kmol/m^3$)
c_{OH^-}	Molar concentration of hydroxide ion in the liquid phase ($kmol/m^3$)
$c_{CO_3^{2-}}$	Molar concentration of carbonate ion in the liquid phase ($kmol/m^3$)
C_D	Drag coefficient
d	Diameter of the droplet (m)
D	Diameter of the absorber (m)
d_0	Diameter of the nozzle hole (m)
d_{32}	Sauter mean diameter (m)
$D^m_{CO_2,G}$	Diffusivity coefficient of CO_2 in the gas phase mixture (pure air) (m^2/s)
$D^m_{w,g}$	Diffusivity coefficient of water in the gas phase mixture (pure air) (m^2/s)
$D^m_{CO_2,L}$	Diffusivity coefficient of CO_2 in the liquid phase mixture (m^2/s)
ρ_G	Density of the gas phase (calculated from the ideal gas law) (kg/m^3)
ρ_L	Density of the liquid phase (kg/m^3)
ε_L	Volumetric fraction of the liquid inside the absorber
E_c	Energy consumption (kWh/tCO_2)
E_c^{exp}	Energy consumption determined experimentally (kWh/tCO_2)
E	Enhancement factor
$\dot{F}_L$	Volumetric flow rate of the liquid phase (m^3/s)
$\dot{G}$	Molar flow of gas ($kmol/s$)
g	Standard acceleration of gravity (m/s^2)
γ_w	Activity coefficient of water in the liquid mixture
H	Total height of the absorber (m)
H_{OG}	Height of transfer unit (m)
H^{exp}_{OG}	Height of transfer unit determined experimentally (m)
H^{mod}_{OG}	Height of transfer unit determined with the model (m)
H_{v,CO_2}	Henry constant to describe the solubility of CO_2 in the liquid mixture ($Pa*m^3/kmol$)
Ha	Hatta number
$k^c_{G,w}$	Local (equal to overall) mass transfer coefficient of water in the gas phase (m/s)
k^c_{G,CO_2}	Local mass transfer coefficient of CO_2 in the gas phase (m/s)
k^c_{L,CO_2}	Local mass transfer coefficient of CO_2 in the liquid phase (m/s)
K^c_G	Overall mass transfer coefficient of CO_2 in the gas phase (m/s)
k	Second order reaction rate constant in the electrolyte mixture ($m^3/(kmol*s)$)
k'	Pseudo first order reaction rate constant in the electrolyte mixture ($1/s$)
$\dot{L}$	Molar flow of liquid ($kmol/s$)
M_{CO_2}	Molecular weight of CO_2 ($kg/kmol$)
μ_G	Viscosity of the gas phase (pure air) ($kg/(m*s)$)
μ_L	Viscosity of the liquid mixture with salts ($kg/(m*s)$)
n	Number of nozzle holes in the nozzle plate
$\dot{N}_w$	Flux of water from the liquid phase to the gas phase ($kmol/(s*m^2)$)
$\dot{N}_{CO_2}$	Flux of CO_2 from the gas phase to the liquid phase ($kmol/(s*m^2)$)
N_{OG}	Number of transfer units or theoretical stages
η_p	Pump efficiency
P	Pressure of the gas phase (Pa)
p_s	Saturation pressure of water (Pa)
ΔP^{exp}_{nozz}	Pressure drop across the nozzle plate determined experimentally (Pa)
R	Universal gas constant ($Pa*m^3/(kmol*K)$)
r	Capture rate ($kgCO_2/(h*m^3 abs)$)
r_{exp}	Capture rate determined experimentally ($kgCO_2/(h*m^3 abs)$)
r_{mod}	Capture rate determined with the model ($kgCO_2/(h*m^3 abs)$)
r_v	Reaction rate ($kmol/(s*m^3)$)
Re_L	Reynolds number of the liquid inside the nozzle
Re_L	Reynolds number of the liquid inside the absorber
S	Mass transfer surface area (m^2)
σ_L	Surface tension of the liquid mixture with salts (J/m^2)
T	Temperature of the system (K)
t_e	Time of exposure between the gas and the liquid phase (s)
t_{flight}	Flight time of the droplets at certain height (s)
ΔV	Infinitesimal differential absorber volume (m^3)
v_G	Velocity of the gas (m/s)
v_L	Velocity of the liquid droplets falling (m/s)
v_0	Injection velocity or velocity of the liquid inside the nozzle hole (m/s)
v^{top}_G	Velocity of the gas at the top of the set-up (m/s)
x_w	Mole fraction of water in the bulk liquid phase
y_{CO_2}	Mole fraction of CO_2 in the bulk gas phase
$y^i_{CO_2}$	Mole fraction of CO_2 in the interface gas phase
$y^*_{CO_2}$	Mole fraction of CO_2 in the gas phase in equilibrium with the bulk liquid phase concentration of CO_2.
$y^{in}_{CO_2}$	Mole fraction of CO_2 in the gas phase at the absorber inlet
$y^{out}_{CO_2}$	Mole fraction of CO_2 in the gas phase at the absorber outlet
y_i	Mole fraction of the component i
y_w	Mole fraction of water in the gas phase
y^*_w	Mole fraction of water in the gas phase in equilibrium with the bulk liquid phase concentration of water.
Δy_{CO_2}	Change in mole fraction of CO_2 in the bulk gas phase
Δz	Infinitesimal differential absorber height (m)
z	Absorber height (m)
z_i	Absorber height at the height step i (m)

technologies involving heating, cooling or pressurizing the air to improve the absorption performance are not feasible (Lackner et al., 1999). Moreover, air pressure drop has become a critical design variable in the CDR technologies (Mazzotti et al., 2013). Any reactor technology involving high pressure-drops, such as the bubble columns, seems to be not economically feasible for DAC of CO_2 with chemicals.

Main operational conditions of the spray and packed towers for CO_2 capture using aqueous NaOH are summarized in Table 1. Special emphasis was placed on the mass transfer parameters such as the effective specific surface area (a_e), the overall mass transfer coefficient (K_G^c), the flux of CO_2 into the liquid phase ($\dot{N}_{CO_2}$) and the height of transfer unit (H_{OG}). Two additional values, namely the specific capture rate or capture rate (r in kg CO_2/(h-m^3 absorber)) and the energy consumption (E_c in kWh/t CO_2), were included as a performance parameters directly related to the capital costs (equipment size) and operational costs, respectively.

In general, spray towers have the lowest specific surface area, which results in small capture rate. Only when using a high CO_2 concentration (not CDR), the capture rate of a spray absorber was comparable to that of packed absorbers (Bandyopadhyay and Biswas, 2012). This was mainly due to the increasing driving force for mass transfer, which results in a higher CO_2 flux. On the other hand, geometric, hydrodynamic and chemical variables could affect the overall mass transfer coefficient. Differences in the reported values in Table 1 are related with the concentrations in the liquid phase and fluid velocities. For the CODA process, the influence of the CO_3^{2-} concentration on the mass transfer coefficient is crucial because the concentration of the solution in the absorber should be close to saturation concentration for a subsequent crystallization process. Previous studies showed that carbonated solutions result in a lower mass transfer coefficient (Ghaffari et al., 2023).

The capture rate is a good performance parameter to compare the different technologies because it considers the effect of the specific surface area and the effect of flux on the process performance. As shown in Table 1, packed towers have the best performance in terms of the rate of absorption for DAC. This is mainly due to the high specific surface areas, which depend on geometric and hydrodynamic parameters of the columns. Even though packed towers can bring up a high specific surface area, pressure drop in the gas phase is always present. In fact, the selection of the packing type and flow arrangement for CO_2 direct air capture seek to reduce the air pressure drop (Keith et al., 2018; Mazzotti et al., 2013), giving the high amount of air required to be processed.

Carbon Engineering has reported the implementation results of a packed air-contactor with cross-flow slab geometry to capture 1 t CO_2/day using KOH solutions (Keith et al., 2018). Fans and packing accounts to approximately 19 % of the capital cost of the air-contactor, each (Holmes and Keith, 2012). Through the fluctuation between high and low liquid flow rates, the pressure drop is minimized by avoiding air-channel constriction in the absorber. Such absorber configuration results in the lowest energy consumption reported with 82 kWh/t CO_2 (for fans and pumps) using KOH as absorbent.

In contrast, spray towers are attractive for DAC because they avoid the cost of packing material and have low pressure-drop for the gas. This kind of absorber is of interest in the CODA process because it allows the safe formation of carbonate crystals along the absorber. If the liquid entering to the absorber is close to saturation and the temperature decreases due to change in weather conditions, $Na_2CO_3{\cdot}10H_2O$ crystals might be formed at ambient conditions during CO_2 absorption. Such crystal formation would cause operational problems (blockage) in a packed absorber. However, one disadvantage of spray towers is the high pressure drop through the spray nozzle, which might increase the pumping cost for the liquid (Treybal, 1980). Moreover, the reported spray columns for CO_2 absorption (see Table 1) have a small specific surface area compared to the packed towers. This is related with the formation of a liquid film when the droplets hit the wall and with droplet coalescence (Stolaroff et al., 2008; Tamhankar et al., 2015; Treybal, 1980). In fact, Carbon Engineering studied the use of this type of absorber (Stolaroff et al., 2008), but it was discarded because the capture rate per unit area was reduced while avoiding coalescence by means of decreasing the liquid flow rate (Mahmoudkhani and Keith, 2009).

A nozzle plate injecting vertically spray droplets of nearly uniform size can avoid the loss of surface area in the spray absorbers (Cho et al., 2018). If the droplet size distribution is narrow, the coalescence caused by the difference in velocities among the droplets (when a bigger/ faster droplet hits a smaller/slower one) could be reduced. Using a vertical

Table 1
Overview of reported process conditions of CO_2 absorption columns using aqueous NaOH.

Type of absorber[a]	v_G(m/s) [G/L vol.]	a_e(m^2/m^3)	K_G^c(mm/s) [c_{NaOH}]	$\dot{N}_{CO_2}$(μmol/(s-m^2)) [c]	H_{OG}(m)[c]	r(kg CO_2/(h-m^3abs))[c]	E_c(kWh/t CO_2)[d]	Reference
Spray (full cone)	0.16 [286]	35	1.09 [0.1 M]	3.9	4.20	0.022	–	(Tamhankar et al., 2015)
Packed (structured)	1.49 2	194 338	3 [2–4 M]	48 85	2.56 1.97	1.255 2.229	327 (only fan) 112 (only fan)	(Mazzotti et al., 2013)
Spray (critical flow atomizer) **0.67 % CO_2**	0.117 [107]	48	1.22 [0.27 M]	339	2.00	2.229	9.5[c] (only pump)	(Bandyopadhyay and Biswas, 2012)
Packed (structured) **Cross flow** [e]	1.6 [2034[f]]	210	1.5 [2 M]	14.8	5.08	0.494	117 (only fan)	(Holmes and Keith, 2012)
Packed (structured)	0.7	250 (ideal)	2.3[b] [3 M]	23[b]	1.22	0.911	177	(Mahmoudkhani and Keith, 2009)
Spray (spiral tip nozzle) **Co-current**	0.4 [6481[c]]	1.95	2.5 [2.5 M]	19.4	82.1	0.012	1199–2462[g]	(Stolaroff et al., 2008)
Packed (random) 380 ppm CO_2	–	313	1.2[b] [1 M]	40	–	0.962	555	(Zeman, 2008)
Packed (structured) 500 ppm CO_2	4.3[b] [946]	500 (ideal)	0.98 [2 M Na^+] sat. in CO_3^{2-}	15	8.80	1.158	190[h]	(Baciocchi et al., 2006)

[a] Counter-current gas–liquid flow unless other specified. Inlet CO_2 concentration ~ 450 ppm unless other specified.
[b] Reported by (Holmes and Keith, 2012) or (G. J. Holmes, 2010).
[c] Calculated from reported values.
[d] Energy required by fan and pump unless other specified.
[e] Optimistic optimized case.
[f] Reported by Keith, 2018 that uses an absorber based on this arrangement.
[g] Experimental range, although the authors claimed that in a full-scale system would be much lower.
[h] Under estimated due to an unfortunate unit conversion error as reported in (Mazzotti et al., 2013).

injection, instead of the classical angle spray injection, the droplet loss by adhesion to the wall can be also reduced. The performance of this novel vertical spray tower was experimentally and theoretically assessed for CO_2 capture using ammonia solutions and high CO_2 concentrations (15 %), reaching capture efficiencies around 95 % (Cho et al., 2018). Yet the potential of the mono-sized droplet absorber seems high, its performance in a system with diluted CO_2 and different chemical system has never been assessed.

The aim of this work is to evaluate the performance of a droplet absorber using vertical injection for the capture of air CO_2 using aqueous NaOH. For this, the experimental and theoretical capture rates of a droplet absorber are compared. Considering that one main drawback of the use of a spray tower for CO_2 capture is the loss of surface area due to droplet coalescence, the capture rate (kg CO_2 absorbed per hour in 1 m^3 absorber) in this work is assessed in three ways: experimental, ideal (no coalescence) and non-ideal (coalescence considered with Computational Fluid Dynamics modeling). With the aim to reduce the capital and operational costs of this CDR technology, the droplet absorber is operated in a co-current mode, in which no fan is required. In this arrangement, the falling droplets induce the airflow inside the absorber, in a similar way like in an ejector venturi scrubber (Atay et al., 1987; Treybal, 1980). The implications of using the proposed absorber in a carbon-negative process to produce soda ash are discussed. The analysis allowed proposing a design of a droplet absorber for the CO_2 DAC in the soda ash production of the CODA project.

2. Methods for experimentation and analysis

2.1. Experimental setup and conditions

The droplet absorber was studied in a loop system as shown in Fig. 1. In this set-up, the air and the liquid could flow in co-current mode and counter-current mode (Fig. 1 shows counter-current mode). Both fluids moved continuously in a closed loop and were in contact only in the absorption section (no. 1 in Fig. 1). The absorption section was a cylinder made of transparent PVC (polyvinylchloride) with 28.5 mm diameter and 1.56 m length. In the counter-current mode, a fan (PAPST 8212 JH4 from ebm-papst St. Georgen GmbH & Co. KG) drove the air flow (red arrows in Fig. 1); while in the co-current mode the droplets falling generated the air flow and the fan was switched off. A ball valve was used to manually set the gas velocity inside the absorber (no. 9). CO_2 (99.9 % from Westfalen AG) was fed (green arrow no. 7 in Fig. 1) before the fan in the counter-current mode and the flow rate was adjusted using a digital gas flow controller (EL-FLOW Select F-201CV-050 from Bronkhorst Deutschland). The gas flow controller was calibrated for CO2 using a high precision film flow meter (HORIBASTEC VP-2). The concentration of CO_2 in the gas mixture was measured by an IR spectrometer (LI-850 from LiCor) able to report also the water concentration. Two gas concentration analyzers were used (no. 5 and 10 in Fig. 1) so that the concentration before and after the droplet absorber column was simultaneously and continuously recorded. In addition, the gas pressure drop across the droplet column was measured using a differential pressure meter (GBEL-LED, Fabr. Briem).

A centrifugal pump (ISM405A from ISAMATEC) (no. 12 in Fig. 1) drove the liquid flow (blue arrows in Fig. 1) through a nozzle plate (no. 2 in Fig. 1), which was made of stainless steel (material number 1.4310). Two different nozzle plates were used in the tests. One nozzle plate had 285 laser-drilled holes of 170 ± 20 μm diameter arranged in concentric circles with 5 mm between each circle and 1 mm between the holes in the circles (here called NP285 nozzle). The other nozzle plate had 841 laser-drilled holes of 180 ± 20 μm diameter arranged in a triangular pattern with 0.9 mm between the holes (here called NP841 nozzle). Sketches and microscopic photos of the nozzles are provided in the Supporting Information (section S.1). The pressure drop across the nozzle plate was measured by a pressure device DPI 304 (no. 16 in Fig. 1).

The liquid flow rate was measured with a rotameter (RAGRM3 from ROTA YOKOGAWA) and the liquid temperature was set using a coil tube heat exchanger controlled by a thermostat (Lauda ProLine RP 845 PL1 Chiller from LAUDA). The rotameter was calibrated for solutions containing NaOH and Na_2CO_3 according to the calculation methods for variable-area flowmeters provided in the VDI/VDE 3513 Part 1 standards (VDI/VDE 3513, 2014). Using the liquid inside the 2L vessel at the bottom of the set-up (no. 11 in Fig. 1), temperature of the liquid was

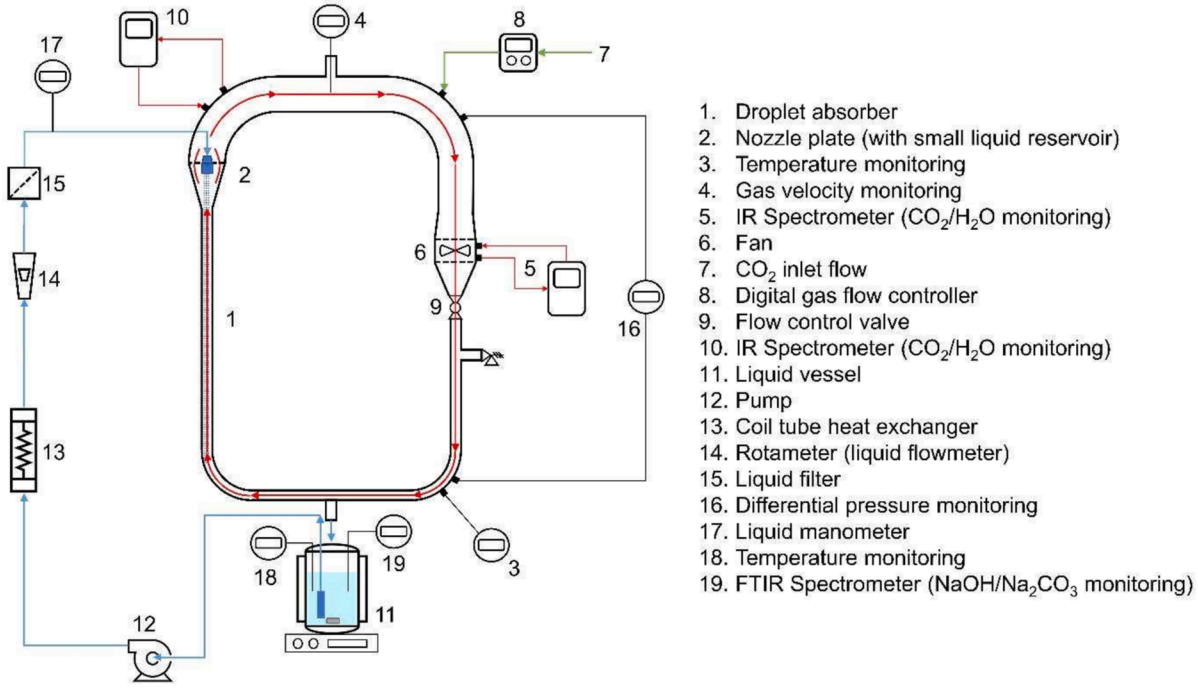

Fig. 1. Scheme of the experimental set-up. Blue line: liquid pathway. Red line: gas pathway in a counter-current mode. (For interpretation of the references to colour in this figure legend, the reader is referred to the web version of this article.)

tracked with a resistive temperature sensor (PT100 and Almemo 2590), while concentration of NaOH and Na_2CO_3 was followed with a FTIR spectrometer (ReactIR 15 from Mettler Toledo). The liquid inside the vessel was homogenized using a magnetic stirrer. A small filter inside the vessel prevented any possible crystals flowing to the pump. The temperature of the gas was also tracked with a resistive temperature sensor (PT100 and Almemo 2590) (no. 3 in Fig. 1) and the gas velocity at the top of the loop (no. 4 in Fig. 1) with a Thermo-Anemometer (405-V1 from Testo).

The performance of the droplet absorber set-up was studied in three different runs: nozzle plate NP285 operated in co-current mode, nozzle plate NP285 operated in counter-current mode (NP285cc) and nozzle plate NP841 operated in co-current mode. Each run consisted of 12 experiments with different conditions of liquid flow rate, CO_2 flowrate, gas velocity, liquid temperature, NaOH concentration and Na_2CO_3 concentration. For each operational variable, three different levels were studied as shown in Table 2. The values for the liquid temperature and concentrations were selected considering the possible conditions in the CODA process, which were previously studied in a previous work (Ghaffari et al., 2023). For each nozzle plate and flow arrangement, a reference experiment (tag "ref") was performed. In other experiments one operational variable was changed and the others were held in the reference experiment value. Exact values of the operational variables used for each experiment are reported in Tables S1 to S3 in the Supporting Information.

A typical run began with an initial solution of NaOH in water at a fixed concentration loaded in the liquid vessel. Then, the flow of liquid was started at the liquid flow rate specified for the experiment. After some minutes, the fan was turned-on (for the counter-current experiment), and the ball-valve was adjusted to have the desired gas velocity at the top (no. 4 in Fig. 1). When the gas velocity was stable (constant for 1 min), the flow of CO_2 was initiated at the specified value. For the experiments where the temperature was changed, the desired value for the temperature was set on the thermostat. The CO_2 concentration in the top and bottom of the absorber was tracked continuously. When the temperature and CO_2 concentration reached a stable point (no change for at least 2 min), the conditions for the next experiments were set. For the experiments where the liquid concentration was changed, the required amount of NaOH or Na_2CO_3 was added inside the liquid vessel.

2.2. Absorber model

The model was based on mass balances on the liquid and gas phases along the absorber. Fig. 2 shows an illustration of the droplet absorber with details on the main variables of the model and the control volumes used for mass balances. The differential equations describing the flow rates and concentrations in the gas and liquid phases are obtained from the mass balances done in the infinitesimal differential volume of height (Δz). To obtain the differential equations, the specific surface area (a) and the cross sectional area (A) were used to account for the surface area for mass transfer (S) in the infinitesimal differential volume (ΔV) (see Equation (2).

$$a = \frac{S}{\Delta V} = \frac{S}{A\Delta z} \tag{2}$$

The global mass balance in the gas phase in co-current mode is presented in Equation (3), which describes the change in the gas mole flow rate ($\dot{G}$) along the absorber. The component mass balances in the gas phase describe the mole fraction change along the absorber (y_{CO_2} for CO_2 in Equation (4) and y_w for water in Equation (5). Details about the mass balance done on the differential volume and its transformation to a differential equation is given in the Supporting Information (section S.3).

$$\frac{d\dot{G}}{dz} = \left(-\dot{N}_{CO_2} + \dot{N}_w\right) aA \tag{3}$$

$$\dot{G}\frac{dy_{CO_2}}{dz} = -\dot{N}_{CO_2} aA - y_{CO_2}\frac{d\dot{G}}{dz} \tag{4}$$

$$\dot{G}\frac{dy_w}{dz} = \dot{N}_w aA - y_w\frac{d\dot{G}}{dz} \tag{5}$$

For the liquid phase, only component balances were done (see Equations (6) to (9). These equations describe the change in concentration of CO_2 (c_{CO_2}), hydroxide ion (c_{OH^-}), water (c_w) and carbonate ion ($c_{CO_3^{2-}}$) along the absorber. The change in the liquid volumetric flow ($\dot{F}_L$) is neglected (change in the volumetric flow rate is around 0.0006 %). The reaction rate (r_v) and the volumetric fraction of liquid in the absorber (ε_L) are needed.

$$\dot{F}_L\frac{dc_{CO_2}}{dz} = A\left(\dot{N}_{CO_2} a - r_v\varepsilon_L\right) \tag{6}$$

$$\dot{F}_L\frac{dc_{OH^-}}{dz} = -2r_v\varepsilon_L A \tag{7}$$

$$\dot{F}_L\frac{dc_w}{dz} = A\left(-\dot{N}_w a + r_v\varepsilon_L\right) \tag{8}$$

$$\dot{F}_L\frac{dc_{CO_3^{2-}}}{dt} = r_v\varepsilon_L A \tag{9}$$

The flux of CO_2 into the liquid phase and the flux of water from the liquid phase were calculated with Eqs. (10) and (11), respectively. The overall mass transfer coefficient was used for CO_2, and the local mass transfer coefficient was used for water (resistance for water mass transfer in the liquid phase was neglected). The concentration gradient was calculated using the CO_2 and water concentrations in equilibrium with the liquid bulk phase concentrations ($y^*_{co_2}$ and y^*_w, respectively). Henry's law was assumed for the phase equilibrium of CO_2 ($y^*_{CO_2}P$ =

Table 2
Operational conditions in the experimental study of the droplet absorber.

Nozzle plate		NP285			NP285cc			NP841		
Flow arrangement		Co-current			Counter-current			Co-current		
Liquid flow rate (L/h)	**Tag**	**Fl-**	**ref**	**Fl+**	**Fl-**	**ref**	**Fl+**	**Fl-**	**ref**	**Fl+**
	Value	38.5	48.2	57.8	38.5	48.2	57.8	116.2	133.6	145.2
CO_2 flow rate (mL/min)	**Tag**	**ref**	**Fco2+**	**Fco2++**	**Fco2-**	**ref**	**Fco2+**	**ref**	**Fco2+**	**Fco2++**
	Value	5.0	6.7	8.4	5.9	6.7	8.4*	7.5*	10	12.6
Gas top velocity (m/s)	**Tag**	**vg–**	**vg-**	**ref**	**ref**	**vg+**	**vg++**	**vg–**	**vg-**	**ref**
	Value	0.21	0.31	0.59	0.15	0.24	0.33	0.20	0.38	0.65
Temperature (°C)	**Tag**	**ref**	**T+**	**T++**	**ref**	**T+**	**T++**	**ref**	**T+**	**T++**
	Value	13.0	15.0	17.5	12.2	14.5	17.2	11.7	14.2	16.8
NaOH (wt.%)	**Tag**	**ref**	**NaOH+**	**NaOH++**	**ref**	**NaOH+**	**NaOH++**	**ref**	**NaOH+**	
	Value	4.8	6.8	9.8	4.8	6.8	9.4	3.7	6	
Na_2CO_3 (wt.%)	**Tag**	**ref**	**Na_2CO_3+**		**ref**	**Na_2CO_3+**		**ref**	**Na_2CO_3+**	**Na_2CO_3++**
	Value	0	2.8		0	2.3		0	5.5	9.7

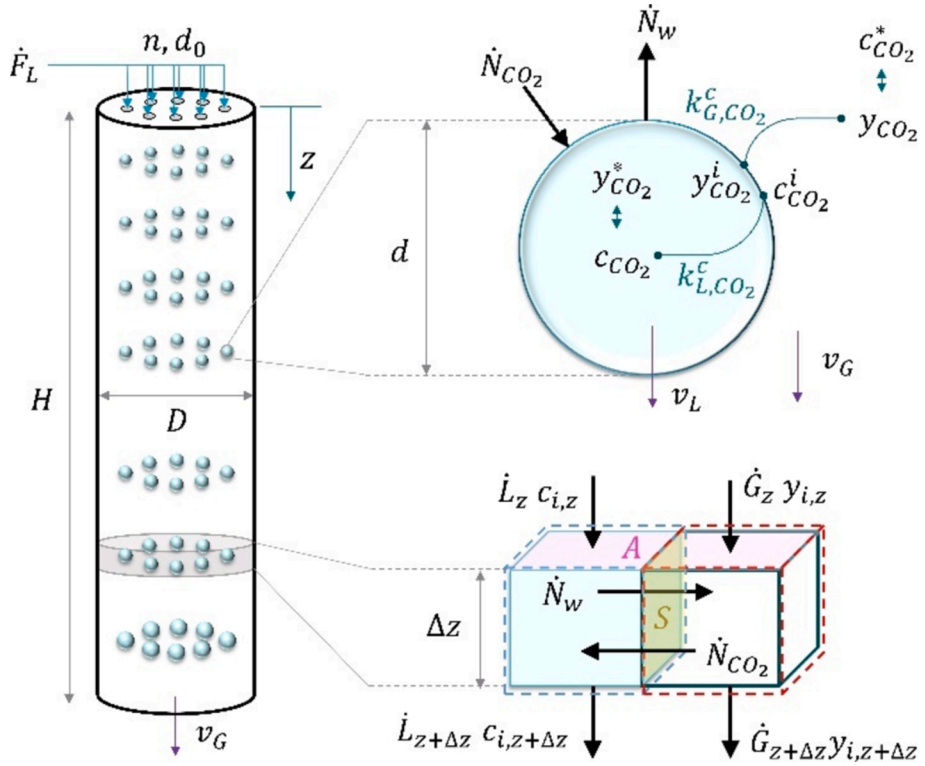

Fig. 2. Illustration of the droplet absorber in the co-current mode used for modeling (gas control volume: red; liquid control volume: blue). (For interpretation of the references to colour in this figure legend, the reader is referred to the web version of this article.)

$c_{CO_2} H_{v,CO_2}$) and an activity model was used for the phase equilibrium of water ($y^*_w P = \gamma_w x_w p_s$). In the last case, the computation of the activity coefficient (γ_w), the mole fraction of water in the liquid phase (x_w) and the water saturation pressure (p_s) is required. The activity coefficient was calculated using the electrolyte NRTL model and the saturation pressure using an empirical correlation as detailed in the Supporting Information (section S.4)

$$\dot{N}_{CO_2} = K^c_G \left(y_{co_2} - y^*_{co_2} \right) \frac{P}{RT} \tag{10}$$

$$\dot{N}_w = k^c_{G,w} \left(y^*_w - y_w \right) \frac{P}{RT} \tag{11}$$

The rate law describing the kinetics of the reaction in Equation (1) is presented in Equation (12), which is a function of the second order kinetic constant (k). The reaction was considered irreversible because the hydroxide ions concentration was always much higher than the concentration of the dissolved CO_2 (Danckwerts, 1970). For the same reason, the concentration of hydroxide ions remains practically constant and the reaction is often assumed as pseudo first order (Gondal et al., 2015a). Then, the rate law is also written using the pseudo-first order kinetic constant (k'), which results from the multiplication between k and c_{OH^-}.

$$r_v = k c_{OH^-} c_{CO_2} = k' c_{CO_2} \tag{12}$$

The overall mass transfer coefficient (K^c_G) has two contributions: one from the mass transfer in the liquid phase and one from the mass transfer in the gas phase. This can be seen in Equation (13), where k^c_{G,CO_2} is the local mass transfer coefficient in the gas phase, H_{v,CO_2} is the Henry volatility constant, k^c_{L,CO_2} is the local mass transfer coefficient in the liquid phase without reaction, E is the enhancement factor of the mass transfer due to the reaction, R is the universal gas constant and T is the temperature of the system.

$$\frac{1}{K^c_G} = \frac{1}{k^c_{G,CO_2}} + \frac{H_{v,CO_2}}{E k^c_{L,CO_2} RT} \tag{13}$$

The local mass transfer coefficient in the gas phase for CO_2 was calculated with a correlation (Equation (14)), known as Froessling's equation, describing the mass transfer coefficient for convective flow surrounding spheres (Bird et al., 2001). Different fluid properties such as the diffusivity of CO_2 in the gas mixture ($D^m_{CO_2,G}$), the gas phase density (ρ_G) and gas phase viscosity (μ_G) are required; as well as operational parameters such as the gas velocity (v_G), the liquid velocity (v_L) and the droplet diameter (d). In the counter-current mode, the sign of the gas velocity is negative due to the upward direction of the flow. The same equation was used for the local mass transfer coefficient in the gas phase for water, using the respective water diffusivity.

$$k^c_{G,CO_2} = \frac{D^m_{CO_2,G}}{d} \left(2 + 0.6 \left(\frac{\rho_G d (1-\varepsilon_L) |v_G - v_L|}{\mu_G} \right)^{0.5} \left(\frac{\mu_G}{\rho_G D^m_{CO_2,G}} \right)^{1/3} \right) \tag{14}$$

The Enhancement factor in Equation (13) is a function of the Hatta number (Ha) and a specific expression is required depending on the reaction regime in the system. For intermediate fast reactions ($0.3 < Ha < 3$), the analytical expression to calculate the Enhancement factor according to the penetration theory or Higbie's model is given by Equation (15) (Danckwerts, 1970; Van Swaaij and Versteeg, 1992). When the reaction is very fast ($Ha > 3$), the enhancement factor is equal to the Hatta number ($E = Ha$). The Hatta number was calculated with Equation (16), in which the pseudo-first order kinetic constant, the diffusivity of CO_2 in the liquid mixture ($D^m_{CO_2,L}$) and the mass transfer coefficient without reaction are required.

$$E = Ha \left[\left[1 + \frac{\pi}{8Ha^2} \right] \mathrm{erf} \sqrt{\frac{4Ha^2}{\pi}} + \frac{1}{2Ha} \exp\left(-\frac{4Ha^2}{\pi} \right) \right] \tag{15}$$

$$Ha = \frac{\sqrt{k' D_{CO_2,L}^m}}{k_{L,CO_2}} \tag{16}$$

The local mass transfer coefficient in the liquid phase without reaction was calculated with Equation (17) based on the penetration theory (Higbie, 1935). In this equation, the time of exposure between the gas and the liquid phase (t_e) was calculated with Equation (18), which uses the droplet diameter and the relative velocity between liquid and gas. The droplet diameter was considered constant (no coalescence) in the ideal case; while in the non-ideal case, it was calculated by Computational Fluid Dynamics (CFD) simulation along the absorber. The time of exposure corresponds to the time required for a gas lump (with v_G) to move from the top to the bottom of a liquid droplet (with v_L) with a certain diameter (d).

$$k_{L,CO_2}^c = 2\sqrt{\frac{D_{CO_2,L}^m}{\pi t_e}} \tag{17}$$

$$t_e = \frac{d}{|v_G - v_L|} \tag{18}$$

In order to have a vertical injection of droplets (avoiding coalescence), the Rayleigh jet breakup regime in the formation of the droplets should be ensured (Huimin Liu, 1999). In this regime, the Reynolds number ($Re_L = d_0 v_0 \rho_L / \mu_L$) and the Ohnesorge number ($Oh = \mu_L / (\rho_L \sigma_L d_0)^{0.5}$) have a certain relation (shown in Fig. S3 in the Supporting Information). The selection of the liquid volumetric flow rate in each experiment was done to ensure the operation in the Rayleigh jet breakup regime. This condition represents a limitation in the operational window of the droplet absorber.

The Henry volatility constant and the second order kinetic constant were calculated as a function of the solution ionic strength, as reported by (Weisenberger and Schumpe, 1996) and (Pohorecki and Moniuk, 1988), respectively. This allowed considering the non-idealities of the liquid phase due to the presence of ions, without the need of an activity coefficient model. The parameters for the Henry constant were taken from (Gondal et al., 2015b) and (Gondal et al., 2015a), respectively. Details on the calculation of the kinetic constant and physical properties needed in the model are presented in Table S4 in the Supporting Information.

2.3. Ideal case

In the ideal case, all droplets have the same size, there is no size dispersion caused by the nozzle; therefore, there is no coalescence inside the absorber. After jet breakup in the Rayleigh regime, the liquid jet (at the length of $4.51 d_0$, where d_0 is the nozzle size) is converted into a spherical droplet so that $d = 1.89 d_0$ (Huimin Liu, 1999). This diameter was used in the calculations of the ideal case.

The expression to calculate the ideal specific surface area in the ideal case is presented in Equation (19), where t_{flight} refers to the flight time of the droplets at height z. This equation was obtained assuming spherical droplets and is based on the expression reported in the literature (Dimiccoli et al., 2000) to calculate the interfacial surface area in a spray absorber. According to this reference, t_{flight} is calculated by solving the differential equation system that describes the droplet falling speed and the droplet flight path.

$$a = \frac{6 \dot{F}_L t_{flight}}{dAz} \tag{19}$$

In the literature, it is mostly assumed that the droplets fall at constant terminal velocity relative to the gas flow (Cho et al., 2018; Stolaroff et al., 2008). However, after comparisons with our CFD simulations, we found that this results in an over estimation of the liquid velocity (see Fig. S4 in the Supporting Information). Using another approach (Dimiccoli et al., 2000) showed a better description of the liquid velocity (using as reference the CFD simulation, see Fig. S4 in the Supporting Information). In this approach, the liquid and gas velocities along the absorber are calculated by solving a system of three differential equations: the first obtained from the forces balance on the liquid, the second expressing the uniformly accelerated motion and the third obtained from the forces balance on the gas (equations (20), 21 and 22). The third equation has been used in the literature to model the induced airflow velocity of falling materials (Li et al., 2015). In the force balance on the gas, the gravitational effect on the air and the friction with the walls of the equipment were neglected. The comparison of the liquid and velocity profiles obtained from the solution of these differential equations and from the CFD simulations allowed validating the use of this model to describe the driving of the airflow by the fall of the droplets in the absorber. Details on the procedure of obtaining these equations are presented in section S.6 in the Supporting Information.

$$\frac{dv_L}{dt} = g\frac{(\rho_L - \rho_G)}{\rho_L} - 3C_D(v_L - v_G)^2 \frac{\rho_G}{4\rho_L d} \tag{20}$$

$$\frac{dz}{dt} = t\frac{dv_L}{dt} + v_0 \tag{21}$$

$$\frac{dv_G}{dt} = \frac{3C_D(v_L - v_G)^2 \dot{F}_L}{A v_G d} \tag{22}$$

To solve these ordinary differential equations (ODEs), the drag coefficient (C_D) is calculated as a function of Reynolds ($Re_L = d|v_L - v_G|\rho_L/\mu_L$) as shown in Equation (23). The three initial conditions are: $z(0) = 0$, $v_L(0) = v_0$ and $v_G(0) = 0$, where is v_0 the injection velocity. The injection velocity depends on the liquid volumetric flow rate, the nozzle size and the number of nozzles (n) as shown in Equation (24).

$$\log C_D = 1.355 - 0.806 \log Re_L + 0.0817 (\log Re_L)^2 \tag{23}$$

$$v_0 = \frac{\dot{F}_L}{n\pi d_0^2/4} \tag{24}$$

The set of differential equations is integrated for each z_i along the absorber using an initial value problem solver on NumPy in Python (since the solution $z = z_i$ is given). The liquid and gas velocities are obtained at $z = z_i$ after integration. The flight time used in Equation (19) is given by the solution of this ODE system and corresponds to the time when $z = z_i$. For the counter-current case, the gas velocity was assumed constant along the absorber and equal to the average velocity calculated from the continuity equation ($v_G A = v_G^{top} A^{top}$).

2.4. Non-ideal case

In the non-ideal case, values for d, v_L, a, v_G and P were extracted from a CFD simulation and its variation along the absorber was considered in the main model. One CFD simulation was done per each nozzle plate in the co-current arrangement using the conditions presented in Table 3. The numerical computations have been performed in the commercial

Table 3
Geometric and process parameters used in the CFD simulations of the droplet absorber in a co-current flow arrangement.

Parameter	NP285	NP841
Nozzle pattern	Concentric, layer space: 2.5 mm	Triangle
Space between nozzles	1 mm	0.9 mm
Number of nozzles (n)	285	841
Nozzle diameter (d_0)	170.2 μ m	179.8 μ m
Volumetric flow rate ($\dot{F}_L$)	60.5 L/h	130 L/h
Injection Velocity (v_0)	2.6 m/s	1.7 m/s
Droplet size at injection	320 μ m	338 μ m

tool Simcenter STAR-CCM+, version 2020.1, Siemens 2020. The CFD simulations were constructed in the same way as presented in a previous publication (Vhora et al., 2024), in which the droplet size distribution along the absorber was measured and compared with the results of CFD simulations. The geometry of the absorber in this case is cylindric and the complete closed loop was simulated (see Fig. S5 in the Supporting Information). The volumetric domain based on the provided geometry was partitioned into discrete cells to establish a computational mesh (also observed in Fig. S5 in Supporting Information).

The governing equations considering turbulent flow conditions were discretized using the finite volume method. The Reynolds-Averaged Navier-Stokes (RANS) equations were applied using the k-ω Menter SST two-layer turbulence model. This model was specifically chosen due to its ability to strike a suitable balance between precision, computational efficiency and robustness (Vhora et al., 2024). The Eulerian-Lagrangian (E-L) framework was used to model the flow of liquid water droplets and the gas phase. This framework involves solving the continuity and Navier-Stokes equations for the continuous gas phase and Newton's second law of motion for the individual liquid droplets. The entire population of liquid droplets was represented with a reduced number of computational parcels. Each parcel consisted of particles assumed to be spherical, sharing identical properties such as diameter, velocity, density, and temperature. This approach facilitates the modeling of turbulent dispersion. Each parcel was treated as a source term integrated into the governing equations of mass, momentum, and energy at its specific location. Furthermore, a computational study to determine the optimal number of droplets within each parcel was done, which enabled to assess its impact on the simulation (Vhora, 2023). No slip boundary conditions were implied on the walls of the configuration. The liquid injection was considered as velocity inlet condition, while the outlet at the bottom was defined as pressure outlet.The collision model used in the software was the NTC (no time counter).

The size of the mesh and the number of parcel streams were selected to ensure that the simulation results are independent of these parameters (Vhora, 2023). The simulation was run until the surface area and gas velocity on the top were constant along the physical time (see Fig. S6 in the Supporting Information). From the CFD simulation results, the droplet size, droplet velocity, gas absolute pressure, droplet surface area and gas velocity were extracted. The total height of the absorption region was divided into segments of 10 mm height. The average of the property for each segment was calculated, except for the specific surface area and the droplet diameter. For the specific surface area, the total surface area of each segment (sum of surface droplets areas) was divided into the segment's volume. For the droplet diameter, the Sauter Mean Diameter or d_{32} was calculated using Equation (25) for the droplet population in sections of 10 mm height. The variation of the property in the radial direction was quantified by the standard deviation.

$$d_{32} = \frac{\sum_i n_i d_i^3}{\sum_i n_i d_i^2} \tag{25}$$

2.5. Experimental case

As shown in Equation (26), the mass balance in Equation (6) can be simplified after neglecting the changes in $\dot{G}$ along the absorber (less than 0.01 %) and assuming that the equilibrium concentration is zero, like described in literature (Mazzotti et al., 2013). With the aim to calculate a performance variable using only experimental values, the molar flow rate is expressed as a function of the gas velocity and the cross-sectional area of the gas flow. The resulting equation was integrated to obtain Equation (27), which was used to calculate the height of a transfer unit (H_{OG}^{exp}) from the experimental results. This variable is often used in engineering to compare equipment for gas–liquid separation. Higher values of H_{OG}^{exp} result in bigger equipment size.

$$\frac{\dot{G}}{A}\frac{dy_{CO_2}}{dz} = -K_G^c a y_{co_2}\frac{P}{RT} \tag{26}$$

$$H_{OG}^{exp} = \frac{v_G}{K_G^c a} = \frac{-H}{\left(1-\frac{n\pi d_0^2/4}{A}\right)\ln\left(\frac{y_{CO_2}^{out}}{y_{CO_2}^{in}}\right)} \tag{27}$$

With the aim to relate the size of the equipment to a certain capture demand, another performance variable was calculated from the experimental results. The experimental capture rate (r_{exp}) was calculated using Equation (28) by using the flow of air, the inlet and outlet concentrations and the total absorber volume. The molar flow was converted into mass flow by means of the molecular weight of CO_2 (M_{CO_2}). The flow of air was estimated from the experimental gas velocity measured at the top (v_G^{top}), the cross-sectional area at the top of the absorber and the gas density.

$$r_{exp} = \frac{\dot{G}}{AH}\left(y_{CO_2}^{in} - y_{CO_2}^{out}\right)M_{CO_2} = \frac{\dot{G}}{AH}\Delta y_{CO_2} M_{CO_2} \tag{28}$$

These performance variables can also be calculated with the model (ideal case and non-ideal case). Both variables change along the absorber because they depend on variables that vary with height; however, only one value was obtained from the experimental data. The height of transfer unit (H_{tOG}^{mod}) and capture rate predicted with the model were calculated as shown in Equations (29) and (30), respectively. In the case of H_{tOG}^{mod}, the values reported in the results section correspond to the logarithmic mean along the absorber. In the case of r_{mod}, the integral of the flow of CO_2 captured ($N_{CO_2} aA$) along the absorber was calculated and divided into the absorber's volume.

$$H_{tOG}^{mod}(z) = \frac{v_G(z)}{K_G(z)a(z)} \tag{29}$$

$$r_{mod} = \frac{\int_0^H \left[K_G(z)a(z)\left(y_{co_2}(z) - y_{co_2}^*(z)\right)\frac{P(z)}{RT}\right]Adz}{AH} \tag{30}$$

Finally, the experimental energy consumption was calculated from the measured pressure drop of the nozzle plate (ΔP_{nozz}^{exp}) and the head required due to the absorber height, as shown in Equation (32). A pump efficiency (η_p) of 85 % was assumed.

$$E_{c,exp} = \frac{\left(\rho_L g H + \Delta P_{nozz}^{exp}\right)\dot{F}_L/\eta_p}{r_{exp}AH} \tag{31}$$

3. Results and discussion

The measured inlet and outlet CO_2 concentrations in the steady state for each experiment are presented in Tables S1 to S3 in the Supporting Information. The concentrations in unsteady state along each experiment are presented in section S.8 in the Supporting Information (Dynamic CO_2 data). The variation of the concentration in the steady state was used to calculate the standard deviation of the measurements. Results on the change in CO_2 concentration between inlet and outlet for all experiments and nozzle plates are presented in Fig. 3.

In general, the co-current operation of the droplet absorber, with the specified geometry, resulted in a change of CO_2 concentration around 112–153 ppm (capture efficiency between 32–36 %). The gas velocity (tag "vg") and the inlet flow of CO_2 (tag "Fco2") had the greatest effect on the change of CO_2 concentration. A slower gas velocity increased the contact time between liquid and gas (residence time of the gas), which resulted in more CO_2 captured. Higher inlet flow of CO_2 resulted in higher inlet concentrations, which increased the driving force for mass transfer causing more CO_2 absorption. In the counter-current operation, the change in CO_2 concentration was around 341 ppm (capture

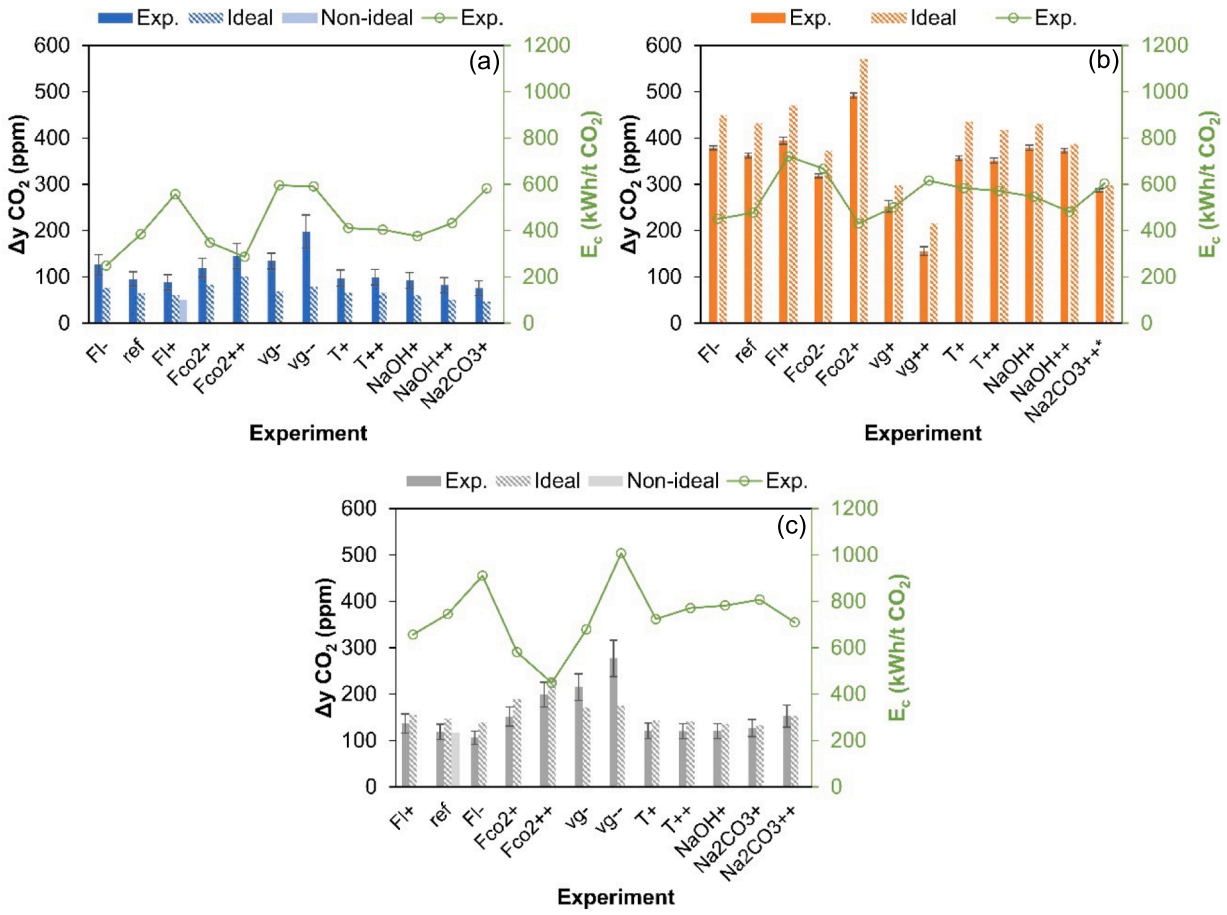

Fig. 3. Change in CO_2 concentration, Δy, and energy consumption, E_c , for the nozzle plates (a) NP285 co-current, (b) NP285 counter-current and (c) NP841 co-current. Exp.: experimentally determined, Ideal: calculated with the ideal model, Non-ideal: calculated with the CFD based model.

efficiency around 65 %), which is considerably higher than that obtained in the co-current operation. However, the capture rate, in terms of mass flow of CO_2 captured per unit volume of absorber, was not necessarily better in the counter-current operation. In fact, since slower gas velocities were handled in the counter-current operation (the gas velocity for the 'ref' tag in the NP285cc was 0.33 m/s, while for the NP285 was 0.59 m/s, as presented in Table 2), the resulting capture rate of most of the experiments was slightly smaller than the one obtained in co-current operation.

The droplet absorber performed similar to packed towers regarding the energy requirement. Fig. 3 presents the experimental energy consumption for all nozzle plates calculated with Equation (31). This parameter varied between 248 and 667 kWh/t CO_2 for the NP285 and between 449 and 1007 kWh/t CO_2 for the NP841. Even though the counter-current operation resulted in bigger change of CO_2 concentration, it also resulted in a bigger energy consumption (comparison between Fig. 3 (a) and (b)). This is not only related with the additional fan energy required in the counter-current operation, but also with the capture rate. The operational variables with the greatest effect on the energy consumption were the liquid flow rate (tag "Fl"), the flow of CO_2 and the gas velocity. While the dependence between the liquid flow rate and the energy consumption is straightforward (pump energy depends linearly with the liquid flow rate, see Equation (31), the effect of the other two variables is explained through the capture rate. An increment of the rate of capture will result in less specific energy consumption.

In the co-current arrangement, the nozzle plate pressure drop (124 ± 17 mbar for the NP285 and 80 ± 8 mbar for the NP841, see Tables S1 and S3 in Supporting Information) represented approximately 43 % for the NP285 and 36 % for the NP841 of the total power consumed. In the counter-current arrangement, the nozzle plate pressure drop represented 42 % and the fan represented 10 % of the total electricity. Therefore, the savings in energy consumption in the co-current arrangement, where the falling of droplets induces the flow of air (no fan needed), are close to 10 %. In comparison with spray absorbers, the nozzle pressure drop of the droplet absorber was considerably smaller (3500 mbar for the spray absorber in (Stolaroff et al., 2008)).

The height of transfer unit of the droplet absorber obtained from the experimental and model results is presented in Fig. S9 in the Supporting Information. For the co-current operation of the droplet absorber, the height of transfer unit was around 4 m, which is similar to that reported for cross-flow packed absorbers (see Table 1). On the other hand, the counter-current operation of the droplet absorber resulted in smaller H_{OG} values, around 1.6 m, which is in the range of the values reported for counter-current packed absorbers. The higher height of transfer unit obtained in the counter-current operation is related with the smaller velocities handled in this arrangement. As in the case of the change of CO_2 concentration, the smaller H_{OG} is not necessarily a better absorption in terms of capture rate. In fact, the smaller gas velocity that results in a smaller height of transfer unit also causes a smaller flow of air processed or less CO_2 absorbed per unit of time.

With the aim to improve the comparison of the capture performance among the experiments and with other absorbers, the absorber capture rate was calculated with Equation (28) (using the concentration and the gas top velocity experimental results). Other variables such as capture efficiency have been used in the literature (Cho et al., 2018; Lim et al., 2013) to evaluate the performance of the absorption. However, the

capture rate was preferred over the capture efficiency and the change in CO_2 concentration because it accounts not only for how much CO_2 is captured, but also for how fast is the capturing. The flux has been also used as performance variable to assess the CO_2 absorption (Holmes, 2010). This variable allows calculating the surface area needed for a certain capture demand and requires additional information on the specific surface area to estimate the absorber size. In contrast, the capture rate contains information of both the mass transfer rate and the available surface area for mass transfer. Consequently, this engineering variable can be directly related with the equipment size and the investment cost.

Results on the capture rate for all experiments and nozzle plates are presented in Fig. 4. Experimental values varied between 0.7 and 2.4 kg CO_2/(h-m^3 absorber), which can be compared with the values presented in Table 1 for the absorbers reported in the literature. Error bars on the capture rate were calculated from the propagation of uncertainty of the CO_2 concentration and the gas velocity.

In general, the studied droplet absorber here had a capture rate in the same range of packed absorbers. Consequently, for a certain capture requirement (in kg CO_2/h), the size of the commercially available packed absorber and the here studied droplet absorber will be very similar. In contrast, while comparing with spay absorbers operating with air CO_2 concentration, the capture rate obtained in the droplet absorber was 100 times higher. The main reason for the high capture rate obtained in the droplet absorber is the higher specific surface area. As it will be discussed in the following sections, the use of a vertical injection, instead of an angle spray injection, allowed obtaining high specific surface areas in the droplet absorber. In addition, the evaluation of the ideal case and non-ideal case models and the discussion on the influence of each independent operational variable on the capture rate will be given in the following sections.

3.1. Model assessment

Fig. 3 and Fig. 4 present the change in CO_2 concentration and capture rate predicted by the ideal (pattern filled bar) and non-ideal (light colored bar) models. For NP285 co-current operation and NP841counter-current operation, the ideal model overestimates the CO_2 absorption. This is explained by the prediction of higher surface areas in the ideal model, which does not consider coalescence. However, for NP285 co-current the absorption rate predicted by the ideal model is smaller than the experimental one. The reason for this is the prediction of higher gas velocities in the ideal model, which results in smaller residence time on the absorber and less captured CO_2. The ideal model considered a constant gas velocity in the radial direction. The pressure drop caused by the friction with the walls and piping accessories (valve, fan, elbows, joints, etc.) were neglected in the ideal model. Even though the ideal model is predicting higher surface areas, it is also predicting faster gas velocities, which for nozzle plate NP285 is more important and results in smaller capture rate.

With the solution of the differential and algebraic equation system, the concentration and the velocity profiles along the absorber height can

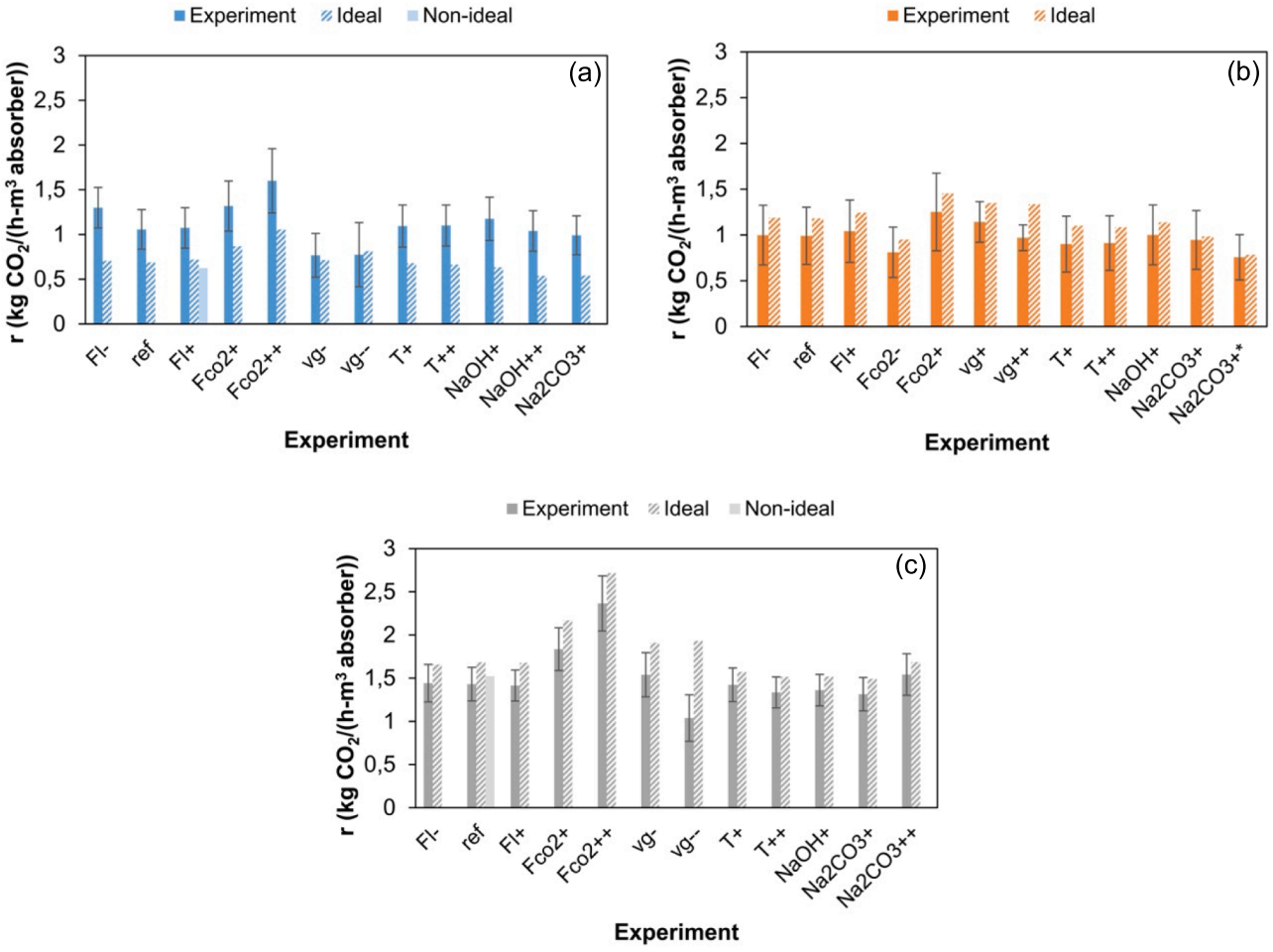

Fig. 4. Capture rate for the nozzle plates (a) NP285 co-current, (b) NP285 counter-current and (c) NP841 co-current. Experiment: experimentally determined, Ideal: calculated with the ideal model, Non-ideal: calculated with the CFD based model.

be obtained. The variation of the CO_2 concentration and the liquid and gas velocities for the co-current arrangement of the nozzle plate NP285 is given in Fig. 5. The concentration profiles for all experiments obtained by the ideal case model are presented in section S.10 in the Supporting Information. Since the ideal case neglects the loss of surface area caused by coalescence, it was expected that this model predicted bigger changes of CO_2 concentration in comparison with the experimental observations. However, both models underestimate the absorption for this nozzle plate, even the non-ideal model that accounts for droplet coalescence. On the other hand, the velocity profiles evidence that the ideal case predicted faster movement of the liquid and gas in comparison with the CFD model. The friction of the gas with the walls and the change of the droplet size due to coalescence were accurately described by the CFD simulation and caused the reduction of the gas and liquid velocities along the absorber. The neglecting of these phenomena in the ideal case predicted of faster liquid and gas velocities.

A deeper analysis into the model allowed explaining the unexpected underestimation of the absorption given by both models for the nozzle plate NP285. Since the gas velocity is directly related with the residence time of the gas inside the absorber, it directly affects the amount of CO_2 captured. Faster gas movement produces smaller residence time on the absorber and less captured CO_2. Both models, the ideal case and the CFD simulation, predicted faster gas velocities because the loss of gas momentum due to the presence of the valve and the fan (number 6 and 9 in Fig. 1) were not considered. This caused the underestimation of the CO_2 capture observed in Fig. 5.

Even though the ideal case predicts a higher gas velocity than the CFD simulation, it also predicts a slightly higher CO_2 capture (see Fig. 5). At first look, this might seem counterintuitive considering the analysis previously done: higher gas velocities result in less CO_2 capture. However, a deeper analysis of the differences in the prediction of the surface area for mass transfer explains this behavior. As stated in Equation (4), higher specific surface area results in bigger changes of CO_2 concentration along the absorber. For the non-ideal case, the coalescence was considered and the surface area available for mass transfer was less than the one predicted in the ideal model. Fig. 6 presents the specific surface area along the absorber for both nozzle plates predicted by the ideal case and by the CFD simulation. For the NP285, there is a small overestimation of the surface area in the ideal case, which explains why the predicted outlet CO_2 concentration with this model is slightly smaller than that of the CFD based model.

The concentration and velocity profiles calculated by both models for the co-current operation of the nozzle plate NP841 are presented in Fig. 7. In this case, the ideal model overestimates the absorption and the non-ideal model produces an estimation very close to the experimental observations. Even though the gas velocity overestimation is also

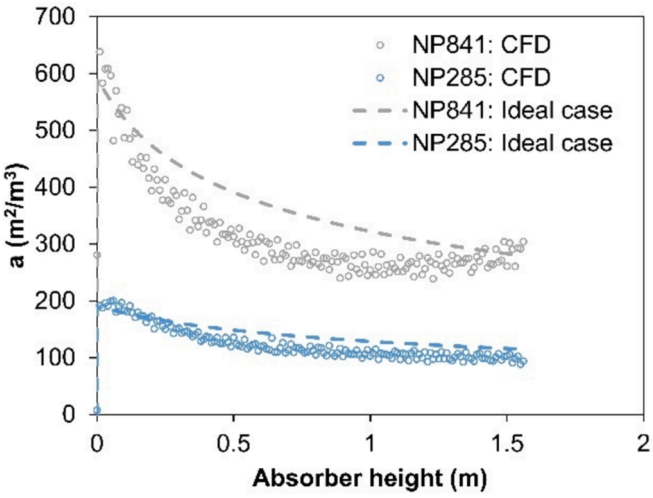

Fig. 6. Specific surface area along the absorber obtained with CFD simulations and the ideal model in the co-current arrangement. Conditions equivalent to "Fl+" experiment for NP285 and to "ref" experiment for NP841.

expected for the nozzle plate NP841, both models are not predicting less CO_2 capture in comparison with the experiments. In this nozzle plate, the loss of momentum due to the fan and the valve is less because more uniform and faster gas velocity profiles are developed when more droplets are generated. As a result, the overestimation of the gas velocity for the nozzle plate NP841 is less than for the NP285, and the consequent underestimation of the CO_2 capture is also reduced.

In addition, the loss of mass transfer area due to coalescence plays a more important role for the nozzle plate NP841 than for the NP285. As evidenced in Fig. 6, the change in the surface area along the absorber is higher for the nozzle plate NP841 than for NP285. The specific surface area for the NP285 decreased from 200 to 90 m^2/m^3, while for the NP841 decreased from 640 to 290 m^2/m^3. The change of the Sauter mean diameter and of the number of droplets along the absorber for both nozzle plates is presented in Fig. S10 in the Supporting Information. Results showed that the number of droplets decreased 74 % for the nozzle plate NP841 and 70 % for NP285. In the same way, the Sauter mean diameter increased by 111 μm for the NP841 and by 63 μm for the NP285. This result is expected since the number of holes is higher and the space between nozzle holes is smaller for the NP841 than for the NP285. Therefore, the probability of droplet collision and coalescence is higher for NP841 than for NP285. In fact, the deviation between the ideal case and the CFD simulation in the description of the specific

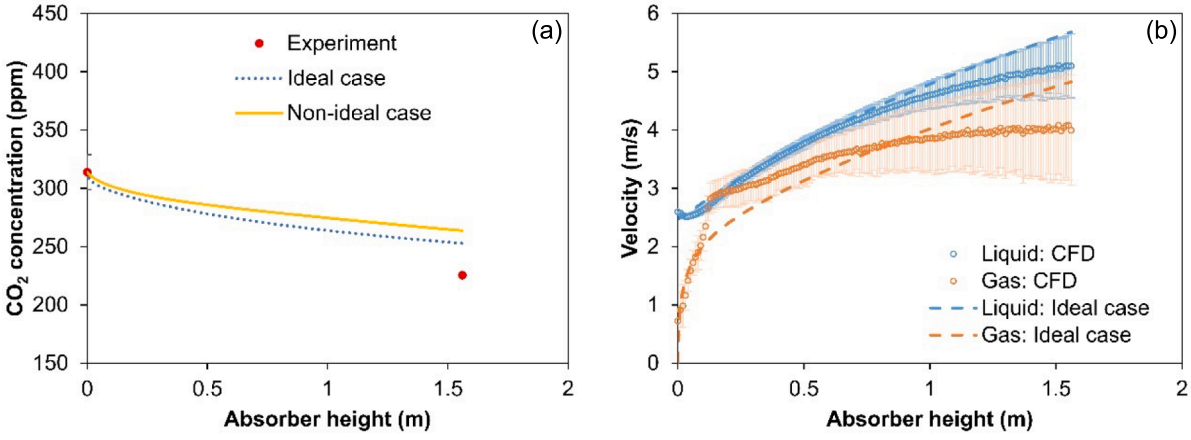

Fig. 5. Model comparison in terms of (a) CO_2 concentration and (b) liquid and gas velocities along the absorber for the NP285 co-current for the "Fl+" experiment.

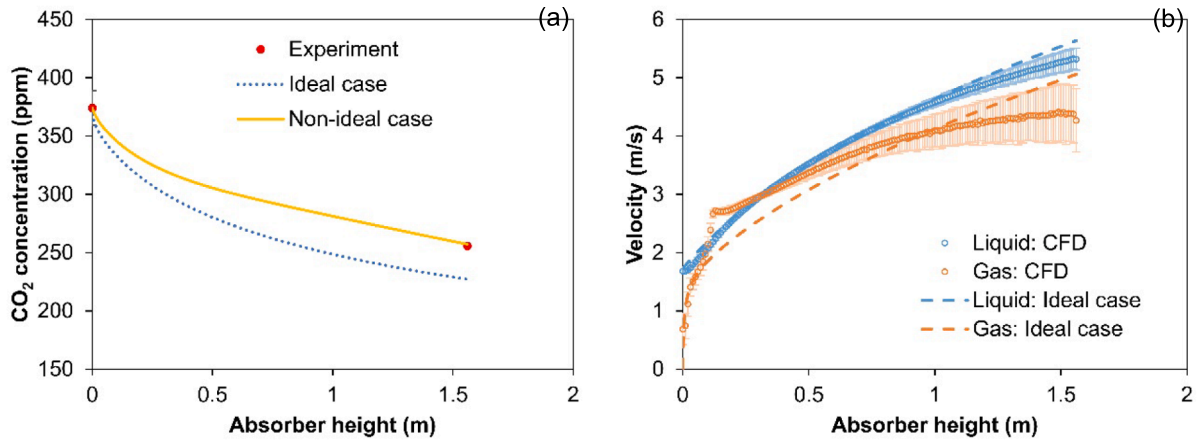

Fig. 7. Model comparison in terms of (a) CO_2 concentration and (b) liquid and gas velocities and along the absorber for the NP841 co-current for the "ref" experiment.

surface area along the absorber is bigger for NP841 because coalescence becomes more important.

Even though the ideal case model is considerably less complex and detailed than the CFD simulation, it is able to describe the decrease in surface area along the absorber. Interestingly, the decrease in the surface area is not only related with the change in droplet size and the number of droplets, but also with the fluid dynamics of the system. The flight time used in Equation (19) implicitly contains information about the liquid velocity. Since the liquid velocity is changing non-linearly along the absorber, the local residence time and the surface area also vary along the absorber. Faster droplets result in shorter flight times and smaller specific surface area. Even though, the droplets transfer some of their energy to the gas, the liquid velocity increases along the absorber because the gravity force accelerates the droplets while falling. Since the net effect is the increasing of the liquid velocity along the absorber, the time of flight and the surface area are reduced.

Through the proper selection of the nozzle size and the liquid flow-rate, a significantly high specific surface area was obtained for the droplet absorber in this study. While for the reported spray absorbers the specific surface area was maximum 48 m^2/m^3, the values obtained in this work varied between 100 and 400 m^2/m^3. These values are in the range of the specific surface area used in the packed absorbers (Table 1). The vertical injection of the droplets allowed reducing the loss of surface area due to the collision with the wall. The specific surface areas predicted by the model for all experiments are presented in Fig. S11 in the Supporting information. For the ideal case model, the logarithmic mean value along the absorber was obtained, and for the non-ideal case, the total surface area calculated with the CFD simulation results was used. The generation of higher surface areas in the NP841 is obtained at the expense of a greater energy dissipation. Higher flow rates should be handled when the nozzle plate has more nozzle holes. The trade-off between capture rate (capital cost) and energy consumption (operational cost) can be recognized in Fig. 3 and Fig. 4. An improvement in the capture rate, which represents smaller absorbers (less capital cost), comes with an increase energy consumption (more operational costs).

In contrast with packed absorbers, the liquid and the gas velocities are tightly related in the operation of the droplet absorber in the co-current arrangement. The ideal case and the CFD simulation results allowed closely observing this relation (see Fig. 4(b) and Fig. 6(b)). According to the CFD simulation results, in the first 0.12 m of absorber the gas velocity is rapidly increased until reaching the liquid velocity. The discontinuity observed in the gas velocity is due to the change in the geometry of the absorber, which changes from a conical shape into a cylindrical one (see Fig. S5 in the Supporting Information). After this height, the liquid velocity is bigger than the gas velocity and this difference is increased continuously along the absorber. Even though the model proposed in this study does not describe the velocity profiles with the same precision as the CFD simulation, it allowed obtaining a proper description of the liquid and gas velocities inside the droplet absorber. In fact, the velocities predicted in the ideal case model are within the standard deviation of the velocities obtained by the CFD simulation. As discussed above, the proper prediction of the fluid dynamics inside the droplet absorber is a key factor in the description of the capture performance.

3.2. *Influence of the CO_2 inlet concentration*

In the process concept of the CODA project, the CO_2 concentration of the inlet gas is close to 400 ppm because the absorber uses CO_2 directly from air. The CO_2 concentration in air was 410 ppm in the year 2019 (IPCC, 2023) and it is estimated that in the year 2060 this concentration will increase up to 637 ppm (IPCC, 2001). With the aim to observe the effect of this variable on the absorption, the inlet flow of CO_2 was experimentally varied (tag "Fco2" in Table 2, Fig. 3 and Fig. 4). Consequently, the inlet CO_2 concentration varied inside the range from 314 to 687 ppm. Fig. 8 shows graphically the effect of the inlet CO_2 concentration on the capture rate, where it can be observed that the capture rate increases linearly with the inlet CO_2 concentration. This

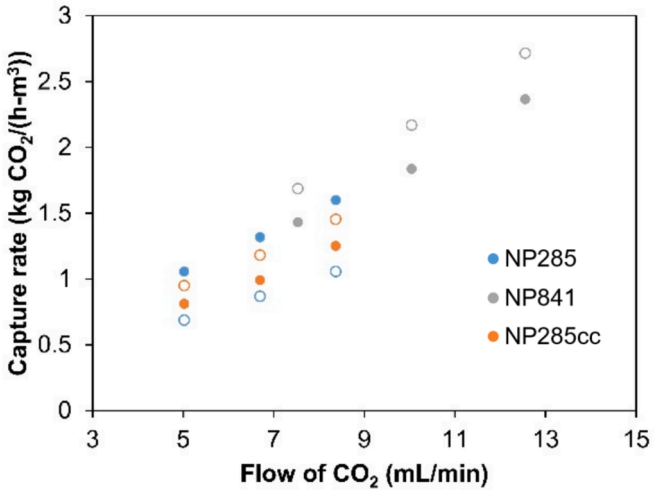

Fig. 8. Effect of the CO_2 inlet concentration on the capture rate of the droplet absorber for different nozzle plates. Experimental (filled markers) and model (empty markers) values.

behavior has been reported previously in the literature for packed absorbers (Holmes, 2010), using the CO_2 absorption flux as performance variable. When the inlet CO_2 concentration is increased by 50 ppm, the capture rate (productivity) is increased by approximately 10 %. Since the capture rate is increased, the energy consumed (in kW-h) per CO_2 absorbed (in kg) is reduced (see Equation (31), where the capture rate is in the denominator). Consequently, the energy consumption is decreased with higher CO_2 inlet concentrations. In this sense, the droplet absorber (and the packed absorber of the literature) will become more efficient along the years of operation.

In general, the model (empty markers on Fig. 8) is able to describe the effect of the inlet CO_2 concentration on the capture rate of the droplet absorber. However, considerable deviations between the experimental and the model values are observed for the NP 285 in the co-current arrangement. As discussed in the previous section, the underestimation of the capture rate in this nozzle plate is related with the overestimation of the gas velocities inside the absorber.

3.3. Influence of the flow arrangement

According to the results presented in Fig. 3, the change of CO_2 concentration is bigger for the counter-current arrangement than for the co-current. This is mainly caused by the slower air velocities handled in the counter-current operation (higher residence time). However, the capture rate is not higher for the counter-current flow arrangement because the slower air velocities also result in less air processed per unit of time (see gas velocities at the top in Tables S1 to S3 in the Supporting Information). The average experimental capture rate of the NP285 is around 1.11 kg CO_2/(h-m^3 abs) in the co-current arrangement and 0.97 kg CO_2/(h-m^3 abs) in the counter-current arrangement (see Fig. 4). In general, the co-current arrangement resulted in higher experimental capture rate, even though the inlet CO_2 concentration in the counter-current arrangement was around 170 ppm higher than that of the co-current arrangement.

According to the literature, the counter-current arrangement is usually more efficient than the co-current arrangement because of the possibility of generating multiple equilibrium stages in one equipment. However, the co-current flow might be enough for reactive systems, such as in the case of sulfur dioxide absorbers. If a rapid and irreversible chemical reaction with the dissolved solute occurs in the liquid, only the equivalent of one theoretical stage is required (Treybal, 1980). In fact, the theoretical number of stages (N_{OG}) can be calculated with Equation (32), in which the equilibrium concentration ($y^*_{co_2}$) was neglected, like in the literature (Mazzotti et al., 2013). Such assumption can be done in reactive systems where the absorbed component is consumed rapidly by the reaction, and its concentration is kept around zero in the liquid phase. This assumption represents less than 0.7 % of deviation in the estimated number of stages (Fig. S12 in the Supporting information).

$$N_{OG} = -\int_{y_{in}}^{y_{out}} \frac{dy_{CO_2}}{y_{co_2} - y^*_{co_2}} = -\int_{y_{in}}^{y_{out}} \frac{dy_{CO_2}}{y_{co_2}} = -\ln\left(\frac{y^{out}_{CO_2}}{y^{in}_{CO_2}}\right)$$
$$= -\ln\left(1 - \frac{y^{in}_{CO_2} - y^{out}_{CO_2}}{y^{in}_{CO_2}}\right) \quad (32)$$

Equation (32) shows that if the capture efficiency (defined as $(y^{in}_{CO_2} - y^{out}_{CO_2})/y^{in}_{CO_2}$) is less than 63.2 %, the number of theoretical stages is less than one (Fig. S12 in the Supporting information). Therefore, the counter-current arrangement would not represent any advantage to the process, if the capture efficiency were kept under this value. Consequently, other flow arrangements could be used for DAC, providing the additional advantage of having less pressure drop in the gas side.

When the capture efficiency exceeds 80 %, the number of theoretical stages increases exponentially. This is expected since the driving force for the absorption is reduced if the capture efficiency is high. The designed and currently published processes to capture CO_2 directly from air handle capture efficiencies around 56 % for counter-current packed absorbers (Mazzotti et al., 2013) and around 74 % for crossflow packed absorbers (Keith et al., 2018). The results obtained in this study suggest that the capture efficiency in a droplet absorber operated in co-current arrangement should be kept below 63.2 % to obtain the best performance. In this way, the capture rate could be equivalent to (and even better than) that of the counter-current droplet absorber and the energy consumption would be 10 % smaller because the fan energy is not needed.

3.4. Influence of the liquid and gas flow rates

In each run, three different levels of liquid flow rate (tag "Fl" in Table 2, Fig. 3 and Fig. 4) and of gas velocity (tag "vg" in Table 2, Fig. 3 and Fig. 4) were tested. In the co-current arrangement, the variation of the liquid flow rate produces also a change in the gas velocity because the falling of the droplets induces the gas movement. This variation is described by Equation (22) in the model.

With the aim to obtain a vertical column of droplets and to avoid coalescence, the liquid flow rate was varied only inside the Rayleigh breakup regime. Since this range of variation was small, the liquid flow rate had not significant impact on the capture rate. This can be qualitatively observed in Fig. 4 and quantitatively observed in Fig. S13 in the Supporting Information, where the influence of the liquid injection velocity on the capture rate can be observed. The experimental results showed a slightly higher capture rate at smaller liquid velocities in the co-current operation. This is expected since the smaller liquid flow generated a slower movement of gas, increasing the contact time between liquid and gas. On the other hand, the energy consumption increased linearly with the liquid flow rate (as shown in Equation (27). Consequently, lower liquid flow rates ensuring the droplet formation in the Rayleigh breakup regime are preferred because the capture rate is not significantly affected and the energy consumption can be minimized.

The gas velocity inside the droplet absorber was modified by closing the valve on the right side of the set-up in the co-current operation and by opening the valve in the counter-current operation. The influence of this variable on the capture rate is not clear only by observing Fig. 4 (Fig. S14 in the Supporting Information for a quantitative comparison). According to Equation (28), the capture rate increases linearly with the gas velocity ($\dot{G} = v_G A \rho_G / M_{CO_2}$) and with the change in CO_2 concentration (Δy_{CO_2}). As it could be observed in Fig. 3, the increase the gas velocity results in a smaller Δy_{CO_2} (see Fig. S14 in the Supporting Information for a quantitative comparison). As discussed before, the faster gas flow reduces the contact time between liquid and gas and results in less CO_2 absorbed. As a result, the increment of the gas velocity has two opposite effects on the capture rate: it increases the flow of air processed, increasing $\dot{G}$, and it reduces the change of CO_2 concentration, decreasing Δy_{CO_2}. The resulting effect of the gas velocity on the capture rate would depend on how much is the flow of air processed increased and how much is the change in CO_2 concentration decreased.

In the co-current arrangement, the highest capture rate was experimentally obtained when the average gas velocity was around 2.5 m/s for the NP285 and around 1.7 m/s for the NP841. For both nozzle plates in the co-current operation, the ideal case model was not able to describe the effect of the gas velocity on the change in CO_2 concentration and the capture rate. In this flow arrangement, the gas velocity was calculated from Equation (22), which did not consider the effect of closing the valve in the experiments with tag "vg". On the other hand, in the counter-current arrangement, an average velocity around 1 m/s was required to obtain the highest capture rate. In this arrangement, the ideal case model was able to predict the effect of the velocity on the change in CO_2 concentration but not on the capture rate. The ideal case model here presented could be improved by including the momentum loss produced by the friction with the walls and the accessories outside the absorber section. In this way, the model could be used to find the

optimal gas velocity in which the capture rate is maximized.

3.5. Influence of the temperature and liquid concentration

In a previous work (Ghaffari et al., 2023), the effect of temperature, NaOH and Na_2CO_3 concentration on the mass transfer coefficient was studied under conditions in which no mass transfer limitations are present (high liquid and gas velocities). In the present study, their effect on the absorption was also studied, but mass transfer limitations might have an impact on the results. Three different levels of temperature (tag "T" in Table 2, Fig. 3 and Fig. 4), two levels of NaOH concentration (tag "NaOH" in Table 2, Fig. 3 and Fig. 4) and two levels of Na_2CO_3 concentration (tag "Na2CO3" in Table 2, Fig. 3 and Fig. 4) were studied. Results can be qualitatively observed in Fig. 3 and Fig. 4 (quantitative effects are shown in Fig. S15 and Fig. S16 in the Supporting Information).

In the studied range, the temperature had no significant effect on the capture rate. On the other hand, even though the effect of the NaOH and Na_2CO_3 concentration on the capture rate is small, some trends could be observed. For the co-current operation of the nozzle plate NP285, an optimal NaOH concentration around 6.8 wt% could be observed where the capture rate had the highest value. However, this was not observed for other nozzle plates and was not described by the model. Regarding the Na_2CO_3, the increase of its concentration results in a slight decrease of the capture rate. The deviation of this trend observed for the highest concentration in the nozzle plate NP841 might be caused by the higher temperature observed in this experiment. The addition and dissolution of Na_2CO_3 in this experiment caused the increase of the temperature of the system due to the heat of dissolution. In this study, changes in the liquid density and viscosity due to the changes in the liquid concentration might affect the absorption because the fluid dynamics (droplet formation, induced gas velocity, flow regime, friction loss, etc.) is also affected.

In general, the temperature, NaOH concentration and Na_2CO_3 concentration had no significant effect on the capture rate in comparison with other operational variables such as the liquid and gas velocities. Even though these properties affect the mass transfer coefficient in the same way as described in the previous study (Figs. S17 and S18 in the Supporting Information), the effect of other variables such as specific surface area on the capture rate is more important.

3.6. Practical implementation and further improvement

The comparison of different nozzle plates and flow arrangements guides the design of a droplet absorber for the CODA process to produce soda ash. The co-current arrangement of the droplet absorber is preferred because it represents capital and operational costs savings. For the selection of the nozzle plate, an optimization based on cost analysis is still required. The quantification of the impact of the capture rate increase on the capital costs and the energy consumption decrease on the operational costs will lead the nozzle plate selection.

Experimental results presented in this study showed that the performance of the droplet absorber is comparable to that of counter-current packed absorbers in terms of capture rate and energy consumption. Moreover, in comparison with the cross-flow packed technology implemented for DAC in Carbon Engineering and with spray absorbers studied in the literature, the droplet absorber showed a better performance in terms of capture rate. However, from the energy consumption point of view, the cross-flow packed absorber used in DAC applications has the advantage since it requires considerably less energy than the droplet absorber: 82 kWh/t CO_2 for the cross-flow packed absorber compared with the 248 kWh/t CO_2 for the droplet absorber in the best case. It should be noted that, the comparison is not completely fair because the mentioned cross-flow packed absorber uses KOH as absorption agent, which has been reported to have a higher mass transfer coefficient than NaOH (Holmes and Keith, 2012). Higher mass transfer coefficients result in a higher capture rate and a decrease in the energy consumption. In fact, the fan energy consumption of the cross-flow packed absorber using KOH is reported to be 61 kWh/t CO_2 (Keith et al., 2018), while when using NaOH the energy consumption is around 117 kWh/t CO_2 (calculated from the optimized optimistic case in (Holmes and Keith, 2012)). In the CODA process, the use of NaOH is required to obtain the desired product (soda ash) and a change of absorbent is not an option to reduce the energy consumption.

Decreasing the liquid flow rate would have the biggest potential for decreasing the energy consumption. Since the injection liquid velocity and the nozzle diameter are fixed by the desired droplet formation regime, the remaining option to decrease the liquid flow rate is the reduction of the number of nozzle holes. As observed in this study, a reduction in the number of nozzle holes results in a reduction in the specific surface area and in the capture rate. Therefore, the number of nozzle holes would be an optimization variable because it has an opposite impact on the capital costs (capture rate) and on the operational costs (energy consumption). Other options to decrease the energy consumption of the droplet absorber are the reduction of the nozzle pressure drop or the reduction of the absorber height. In general, the reduction of the energy consumption should be addressed as an optimization problem because the design variables affecting the energy consumption also have an impact on the capture rate.

In contrast with counter-current absorbers, there is no limit on the gas to liquid ratio (G/L) in co-current absorbers (Treybal, 1980). However, in the case of a co-current absorber in which the airflow of air is driven by the fall of droplets, the force balance establishes the G/L ratio. The volumetric G/L ratio handled in the droplet absorber varied from 43 to 142 for the NP285 and for 15 to 48 for the NP841 in the co-current operation. For a practical implementation, the droplet absorber would require higher liquid volumetric flow rate to process the same amount of air compared with packed absorbers (see G/L ratio on Table 1). In this sense, the size of the pumps associated with the droplet absorber would be considerably bigger than in the case of a packed absorber.

On the other hand, an advantage of the droplet absorber over the packed absorber would be that it does not require any packing, which represents saving of capital costs. Moreover, the droplet absorber would be smaller than the cross-flow packed absorber implemented by Carbon Engineering because higher capture rates can be obtained in the droplet absorber. However, for the droplet absorber to be economically feasible in an industrial scale, the production cost of the nozzle plate should be still minimized. For example, a change in the material of the plate would significantly reduce its production cost.

Despite of its relatively high-energy consumption, the droplet absorber here studied has the potential to provide a technically feasible solution in the absorption of CO_2 using liquid NaOH solutions saturated in Na_2CO_3. In such cases, the possible crystallization of sodium carbonate inside the absorber would not represent an operational problem. This would allow to feed the solution out of the absorber to a crystallization train, in which sodium carbonate decahydrate could be crystallized by cooling crystallization or vacuum evaporative crystallization below 37 °C, or sodium carbonate monohydrate could be crystallized by vacuum evaporative crystallization between 40 and 100 °C. Both vacuum evaporative crystallization strategies would require less energy, if the solution out of the absorber is close to saturation. Model-based analysis on the implications of the use of a droplet absorber and the selection of the crystallization strategy on the energy consumption of the CODA process were previously published (Gutierrez et al., 2023). Future publications will focus on the development on the crystallization process and complete CODA process design.

Other possible application of the droplet absorber could be the CO_2 capture from flue gas, in which higher capture rates are expected giving the higher concentration of CO_2 in the inlet gas. However, the presence of a reversible reaction in the system with flue gas (reaction between water and CO_2 to produce bicarbonate) could require a counter-current operation of the droplet absorber. Further studies on the cost-based

optimization of the droplet absorber and on the technical feasibility in other applications are recommended.

4. Conclusion

The experimental and modeling results described demonstrate that the CO_2 capture from air in NaOH solutions for soda ash production in a droplet absorber is a technically feasible strategy that benefits from its specifications. The potential blockage inside a packed absorber caused by Na_2CO_3 crystallization is avoided by the droplet absorber because no packing is used. In this work, the vertical injection of micro-droplets reduces loss of surface area due to droplet collision with the walls, and higher specific surface areas are obtained in comparison with spray absorbers with angle injection proposed in the literature. The capture rate of the droplet absorber was similar to that reported in counter-current packed absorbers and higher than that reported in cross-flow packed absorbers and spray absorbers for DAC. Experimental results and theoretical analysis reveal that the traditional counter-current flow arrangement does not necessarily brings the multi-staging advantages in the CO_2 reactive absorption for DAC applications. In the co-current operation of the droplet absorber, the flow of air is induced by the fall of droplets and no fan is required for this arrangement. As a result, the co-current arrangement could represent capital investment and operational costs savings, but it also links the gas and liquid velocities and defines the G/L ratio on the absorber to a relatively small value. Smaller G/L ratios result in higher liquid flow rates, which increase the energy consumption of the droplet absorber. In fact, results show that the droplet absorber has a higher energy consumption than that reported for packed absorbers. Possible changes in the droplet absorber design that reduce the energy consumption also decrease the capture rate. Consequently, a cost-based optimization of the droplet absorber design is recommended for the proper selection of number of nozzle holes, nozzle diameter, absorber height and diameter. The model developed in this contribution could be used as basis for such optimization study.

CRediT authorship contribution statement

Maria F. Gutierrez: Writing – review & editing, Writing – original draft, Visualization, Validation, Software, Methodology, Investigation, Formal analysis, Data curation, Conceptualization. **Kasimhussen Vhora:** Writing – review & editing, Software, Data curation. **Somayyeh Ghaffari:** Writing – review & editing, Validation, Investigation. **Gábor Janiga:** Writing – review & editing, Software. **Andreas Seidel-Morgenstern:** Writing – review & editing. **Heike Lorenz:** Writing – review & editing, Project administration, Funding acquisition. **Peter Schulze:** Writing – review & editing, Validation, Supervision, Project administration, Methodology, Investigation, Funding acquisition, Conceptualization.

Declaration of competing interest

The authors declare that they have no known competing financial interests or personal relationships that could have appeared to influence the work reported in this paper.

Acknowledgements

The authors acknowledge the financial support by the BMBF (No. 01LJ2003B) and the European Union-NextGenerationEU. We also thank Jan Protzmann for the security and technical insights of the pilot plant absorber.

Appendix A. Supplementary data

Supplementary data to this article can be found online at https://doi.org/10.1016/j.ces.2024.121133.

Data availability

Data will be made available on request.

References

Atay, L., Lewandowski, G., Trattner, R., 1987. Fluid Flow and Gas Absorption in an Ejector Venturi Scrubber. Environmental Progress 6, 198–203.
Azizi, F., Kaady, L., Al-Hindi, M., 2022. Chemical absorption of CO2 in alkaline solutions using an intensified reactor. Canadian Journal of Chemical Engineering 100, 2172–2190. https://doi.org/10.1002/cjce.24420.
Baciocchi, R., Storti, G., Mazzotti, M., 2006. Process design and energy requirements for the capture of carbon dioxide from air. Chemical Engineering and Processing: Process Intensification 45, 1047–1058. https://doi.org/10.1016/j.cep.2006.03.015.
Bandyopadhyay, A., Biswas, M.N., 2012. CO2 capture in a spray column using a critical flow atomizer. Separation and Purification Technology 94, 104–114. https://doi.org/10.1016/j.seppur.2011.11.039.
Bird, R.B., Stewart, W.E., Lightfoot, E.N., 2001. Transport phenomena, Second. ed. Wiley International.
BMBF (Bundesministerium für Bildung und Forschung), FONA (Forschung für Nachhaltigkeit), 2023. CODA – Development of an environmentally friendly process for the production of soda ash [WWW Document]. Funding Measures. URL https://www.fona.de/en/measures/funding-measures/KlimPro/coda.php (accessed 9.23.22).
Cho, M., Lee, S., Choi, M., Lee, J.W., 2018. Novel spray tower for CO2 capture using uniform spray of monosized absorbent droplets. Industrial and Engineering Chemistry Research 57, 3065–3075. https://doi.org/10.1021/acs.iecr.7b05309.
Danckwerts, P.V., 1970. Gas-Liquid Reactions. McGraw-Hill, New-York.
Dimiccoli, A., Di Serio, M., Santacesaria, E., 2000. Mass transfer and kinetics in spray-tower-loop absorbers and reactors. Industrial and Engineering Chemistry Research 39, 4082–4093. https://doi.org/10.1021/ie000137y.
Gaur, A., Park, J.W., Jang, J.H., Maken, S., Lee, J., Song, H.J., 2009. Characteristics of alkaline wastewater neutralization for CO2 capture from Landfill Gas (LFG). Energy and Fuels 23, 5467–5473. https://doi.org/10.1021/ef900615h.
Ghaffari, S., Gutierrez, M.F., Seidel-Morgenstern, A., Lorenz, H., Schulze, P., 2023. Sodium hydroxide-based CO2 direct air capture for soda ash production—fundamentals for process engineering. Industrial and Engineering Chemistry Research 62, 7566–7579. https://doi.org/10.1021/acs.iecr.3c00357.
Gondal, S., Asif, N., Svendsen, H.F., Knuutila, H., 2015a. Kinetics of the absorption of carbon dioxide into aqueous hydroxides of lithium, sodium and potassium and blends of hydroxides and carbonates. Chemical Engineering Science 123, 487–499. https://doi.org/10.1016/j.ces.2014.10.038.
Gondal, S., Asif, N., Svendsen, H.F., Knuutila, H., 2015b. Density and N2O solubility of aqueous hydroxide and carbonate solutions in the temperature range from 25 to 80°C. Chemical Engineering Science 122, 307–320. https://doi.org/10.1016/j.ces.2014.09.016.
Gutierrez, M.F., Schulze, P., Seidel-Morgenstern, A., Lorenz, H., 2023. Parametric study of the reactive absorption of CO2 for soda ash production. In: Kokossis, A.C., Georgiadis, M.C., Pistikopoulos, E. (Eds.), Proceedings of the 33rd European Symposium on Computer Aided Process Engineering, Computer Aided Chemical Engineering. Elsevier, pp. 2935–2940.
Higbie, R., 1935. The rate of absorption of a pure gas into still liquid during short periods of exposure. Transactions of the AIChE 31, 365–389.
Holmes, G., Keith, D.W., 2012. An air-liquid contactor for large-scale capture of CO2 from air. Philosophical Transactions of the Royal Society a: Mathematical, Physical and Engineering Sciences 370, 4380–4403. https://doi.org/10.1098/rsta.2012.0137.
Holmes, G.J., 2010. A carbon dioxide absorpiton performance evaluation for capture from ambient air (Master's thesis, University of Calgary, Calgary, Canada). Retrieved from https://prism.ucalgary.ca doi:10.11575/PRISM/3443.
IPCC, 2001. Climate Change 2001: Synthesis Report.
IPCC, 2023. Climate change 2023: synthesis report.
Keith, D.W., Holmes, G., Angelo, D.S., Heidel, K., 2018. A process for capturing CO2 from the atmosphere. Joule 2, 1573–1594. https://doi.org/10.1016/j.joule.2018.05.006.
Lackner, K., Ziock, H.-J., Grimes, P., 1999. Carbon Dioxide Extraction From Air: Is It An Option? Conference: 24th Annual Technical Conference on Coal Utilization and Fuel Systems. Clearwater, FL (US). Retrieved from: https://www.osti.gov/servlets/purl/770509.
Li, X., Li, Q., Zhang, D., Jia, B., Luo, H., Hu, Y., 2015. Model for induced airflow velocity of falling materials in semi-closed transfer station based on similitude theory. Advanced Powder Technology 26, 236–243. https://doi.org/10.1016/j.apt.2014.10.003.
Lim, Y., Choi, M., Han, K., Yi, M., Lee, J., 2013. Performance characteristics of CO2 capture using aqueous ammonia in a single-nozzle spray tower. Industrial and Engineering Chemistry Research 52, 15131–15137. https://doi.org/10.1021/ie401981u.
Huimin Liu, 1999. Fundamental Phenomena and Principles in Droplet Processes, in: Science and Engineering of Droplets. William Andrew, pp. 121–237.
Mahmoudkhani, M., Keith, D.W., 2009. Low-energy sodium hydroxide recovery for CO2 capture from atmospheric air-Thermodynamic analysis. International Journal of Greenhouse Gas Control 3, 376–384. https://doi.org/10.1016/j.ijggc.2009.02.003.
Mazzotti, M., Baciocchi, R., Desmond, M.J., Socolow, R.H., 2013. Direct air capture of CO2 with chemicals: Optimization of a two-loop hydroxide carbonate system using a

countercurrent air-liquid contactor. Climatic Change 118, 119–135. https://doi.org/10.1007/s10584-012-0679-y.
Pichler, T., Stoppacher, B., Kaufmann, A., Siebenhofer, M., Kienberger, M., 2021. Continuous Neutralization of NaOH Solution with CO2 in an Internal-Loop Airlift Reactor. Chemical Engineering and Technology 44, 38–47. https://doi.org/10.1002/ceat.202000319.
Pohorecki, R., Moniuk, W., 1988. Kinetics of reaction between carbon dioxide and hydroxyl ions in aqueous. Chemical Engineering Science 43, 677–1684.
Shim, J.G., Lee, D.W., Lee, J.H., Kwak, N.S., 2016. Experimental study on capture of carbon dioxide and production of sodium bicarbonate from sodium hydroxide. Environmental Engineering Research 21, 297–303. https://doi.org/10.4491/eer.2016.042.
Stolaroff, J.K., Keith, D.W., Lowry, G.V., 2008. Carbon dioxide capture from atmospheric air using sodium hydroxide spray. Environmental Science Technology 42, 2728–2735. https://doi.org/10.1021/es702607w.
Tamhankar, Y., King, B., Whiteley, J., McCarley, K., Cai, T., Resetarits, M., Aichele, C., 2015. Interfacial area measurements and surface area quantification for spray absorption. Separation and Purification Technology 156, 311–320. https://doi.org/10.1016/j.seppur.2015.10.017.
Tavan, Y., Hosseini, S.H., 2017. A novel rate of the reaction between NaOH with CO2 at low temperature in spray dryer. Petroleum 3, 51–55. https://doi.org/10.1016/j.petlm.2016.11.006.
Treybal, R.E., 1980. Mass-Transfer Operations, Third Edition. McGraw-Hill.
Van Swaaij, W.P.M., Versteeg, G.F., 1992. Mass transfer accompanied with complex reversible chemical reactions in gas-liquid systems: an overview. Chemical Engineering Science 47, 3181–3195.
VDI/VDE 3513, 2014. Variable-area flowmeters: Calculation methods, in: VDI/VDE-RICHTLINIEN. Engl. VDI/VDE-Gesellschaft Mess- und Automatisierungstechnik.
Vhora, K., 2023. CFD Simulation of an Absorber for CO2 Direct Air Capture (Master Thesis). Otto-von-Guericke-Universität Magdeburg, Magdeburg.
Vhora, K., Janiga, G., Lorenz, H., Seidel-Morgenstern, A., Gutierrez, M.F., Schulze, P., 2024. Comparative Study of Droplet Diameter Distribution: Insights from Experimental Imaging and Computational Fluid Dynamics Simulations. Applied Sciences 14, 1824. https://doi.org/10.3390/app14051824.
Weisenberger, S., Schumpe, A., 1996. Estimation of Gas Solubilities in Salt Solutions at Temperatures from 273 K to 363 K. AIChE Journal 42 (1), 298–300.
Yoo, M., Han, S.J., Wee, J.H., 2013. Carbon dioxide capture capacity of sodium hydroxide aqueous solution. Journal of Environmental Management 114, 512–519. https://doi.org/10.1016/j.jenvman.2012.10.061.
Zeman, F., 2008. Experimental results for capturing CO2 from the atmosphere. AIChE Journal 54, 1396–1399. https://doi.org/10.1002/aic.11452.